The magnitudes of multi-physics effects on geothermal reservoir characteristics during the production of enhanced geothermal system

Song, Guofeng; Shi, Yu; Xu, Fuqiang; Song, Xianzhi; Li, Gensheng; Wang, Gaosheng; Lv, Zehao

DOI
10.1016/j.jclepro.2023.140070

Publication date
2023

Document Version
Final published version

Published in
Journal of Cleaner Production

Citation (APA)
Song, G., Shi, Y., Xu, F., Song, X., Li, G., Wang, G., & Lv, Z. (2023). The magnitudes of multi-physics effects on geothermal reservoir characteristics during the production of enhanced geothermal system. *Journal of Cleaner Production*, *434*, Article 140070. https://doi.org/10.1016/j.jclepro.2023.140070

Journal of Cleaner Production 434 (2024) 140070

Contents lists available at ScienceDirect

Journal of Cleaner Production

journal homepage: www.elsevier.com/locate/jclepro

The magnitudes of multi-physics effects on geothermal reservoir characteristics during the production of enhanced geothermal system

Guofeng Song [a], Yu Shi [b,*], Fuqiang Xu [c], Xianzhi Song [c], Gensheng Li [c], Gaosheng Wang [c], Zehao Lv [d]

[a] Department of Geoscience and Engineering, Delft University of Technology, Stevingweg 1, 2628CN, Delft, the Netherlands
[b] Faculty of Geosciences and Environmental Engineering, Southwest Jiaotong University, Chengdu, 611756, China
[c] National Key Laboratory of Petroleum Resources and Engineering, China University of Petroleum (Beijing), Beijing, 102249, China
[d] Petrochina Research Institute of Petroleum Exploration and Development, Petrochina Oil&Gas and New Energy Company, Beijing, 100083, China

ARTICLE INFO

Handling editor: Yutao Wang

Keywords:
Geothermal
Thermo-hydro-mechanical-chemical coupling
Multi-physics effect
Fracture aperture
Quantitative evaluation

ABSTRACT

The multi-physics coupling process during the heat extraction from enhanced geothermal system, encompassing thermo(T)-hydro(H)-mechanical(M)-chemical(C) interactions, plays a pivotal role in changing geothermal reservoir characteristics. However, a comprehensive quantitative assessment of these multi-physics behaviors has been lacking. In this study, a novel approach was proposed to calculate the magnitude of mechanical, chemical, strong mechanical-chemical coupling, and weak mechanical-chemical coupling effects on the variations of reservoir characteristics. In particular, mechanical-chemical coupling effects are quantified for the first time. They are obtained by the fracture aperture difference results across five distinct coupling models (thermo-hydro, thermo-hydro-chemical, thermo-hydro-mechanical, partially-coupled four-field, and fully-coupled four-field models). The findings indicate that mechanical effects lead to an increase in fracture aperture, while chemical effects contribute to its reduction under underbalanced injection conditions. Strong mechanical-chemical coupling effects, exhibiting a negative correlation with chemical effects, conversely result in a diminished fracture aperture. The influences of these effects are investigated from the temporal and spatial perspectives. Temporally, mechanical effects dominate early production while chemical effects become prominent in later stages. Spatially, there mainly exists two zones when stable production: a mechanical-controlled region surrounding injection wells, and a chemical-controlled area distant from the injection wells. Furthermore, sensitivity analysis of injection concentration indicates its alternation changes the reservoir traits and production performance by modifying the magnitudes of chemical and mechanical-chemical coupling effects. This quantification of multi-physics effects offers insights into optimizing injection strategies for better geothermal development. The approach could hold promising potential in other geo-energy scenarios like carbon and hydrogen storage in reservoirs.

1. Introduction

Geothermal energy is gaining increasing attention in response to escalating CO_2 emissions from fossil fuels (Panwar et al., 2011; Sharmin et al., 2023). It remains stable and unimpeded by fluctuations in climate, seasons, or day and night compared to wind and solar energy (Song, X. et al., 2022). Therefore, it can be a pivotal load-shifting energy source on the path to a carbon-neutral society. Hot dry rock (HDR), a distinctive form of geothermal source, holds promise for power generation owing to its high temperatures (depths of 3–10 km with temperatures ≥180 °C) (Baria et al., 1999; Olasolo et al., 2016). Given the dense rock and low water content inside (Olasolo et al., 2016), the enhanced geothermal system (EGS) was proposed for harnessing HDR resources (Lu, 2018; Song, X. et al., 2022). Techniques such as hydraulic fracturing or shearing are employed to create fractures for the construction of an EGS (McClure and Horne, 2014). The fractures serve as primary channels for fluid flow and heat transfer (Sun et al., 2020). The intricate behaviors within fractures cause variations of fracture properties that may result in thermal breakthroughs and a low life span of the project (Prajapati et al., 2021). Therefore, a thorough characterization of reservoir attribute

* Corresponding author.
E-mail address: shiyu@swjtu.edu.cn (Y. Shi).

https://doi.org/10.1016/j.jclepro.2023.140070
Received 30 August 2023; Received in revised form 19 November 2023; Accepted 2 December 2023
Available online 6 December 2023

fluctuations becomes crucial for the adjustment of long-term geothermal development.

Heat extraction in fracture channels in geothermal reservoirs is typically a complicated thermo-hydro-chemical-mechanical (THMC) coupling process as depicted in Fig. 1 (Li et al., 2022; Rathnaweera et al., 2020; Yang et al., 2023). It demonstrates intricate interplay among fluid flow, heat transfer, solute transport, mechanical deformation, and chemical reactions. Cool fluid acquires heat from the rock media. Concurrently, it conveys heat and solutes from the inlet to the outlet. An imbalanced concentration of silica solute can instigate water-rock reactions. Potential mineral dissolution causes the enlargement of the fracture's aperture. Conversely, mineral precipitation engenders its contraction. Furthermore, chemical reactions along the fracture's surface can induce alterations in its mechanical strength. In the meanwhile, the perturbations in temperature and pressure can induce localized stress shifts, thereby engendering mechanical deformation and consequent modifications in the fracture's aperture (Millington and Quirk, 1961). The combined influences of chemical and mechanical deformation lead to alterations in fracture aperture and transmissibility dynamics. As a result, flow velocity, thermal convection, solute diffusion, and pressure dispersion can be notably impacted. This complex interplay within the THMC coupling process significantly shapes the behavior of geothermal reservoirs during thermal extraction (Taron and Elsworth, 2009, 2010).

Previous studies primarily focused on multi-physics modeling for various aspects of EGS, encompassing production analysis (Chen et al., 2018; Mahmoodpour et al., 2022), optimization (Cui et al., 2023; Song et al., 2021), seismic assessment (Anyim and Gan, 2020; Parisio et al., 2019), and reservoir stimulation (Li et al., 2019). Most studies employed multi-physics modeling to predict flow and heat transfer in reservoirs, serving as inputs for optimization algorithms, seismic analysis, and fracturing modules.

The variation of reservoir characteristics remains a prominent area of interest (Pan et al., 2023; Rohit et al., 2023; Zhu et al., 2023). It is crucial for understanding and facilitating efficient geothermal development. However, limited research investigated the contributions of multi-physics effects to reservoir characteristics and production. Ebrahimi et al. (2022) simulated the injection into the EGS based on the THM model. The results showed that poroelastic effects take precedence during the initial stages, while thermoelastic effects come to the forefront during prolonged injection periods. Xu et al. (2023) focused on the mechanical part and presented the fracture damage characteristics and laws according to effective stress, von Mises stress and Tresca stress of rocks for long-term geothermal development. The fracture morphology and volume increased significantly with the increase of temperature and stress difference, and the temperature effect was more obvious. Ji et al. (2023b) found chemical reaction rate determined the fracture deformation under the THC model.

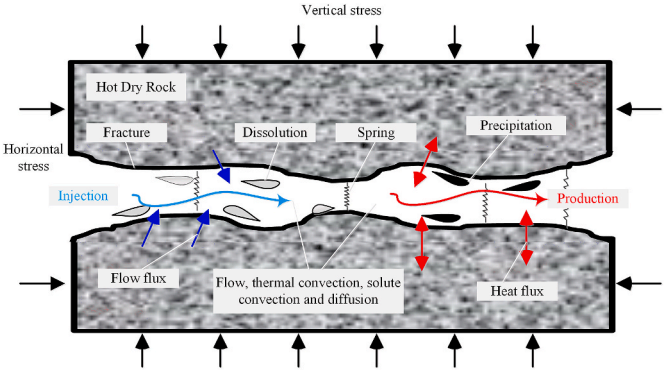

Fig. 1. Multi-physics processes in the fracture during EGS production (Song, G. et al., 2022b).

Actually, it is essential to encompass all potential physical couplings when analyzing reservoir characteristics. This implies the inclusion of the THMC model in the analysis. Salimzadeh and Nick (2019) found THM and C two-way coupling might redistribute the stress to achieve mechanical equilibrium and update aperture distribution. Rawal and Ghassemi (2014) highlighted the minor contribution of thermo-poroelastic processes relative to silica dissolution in driving aperture increment. Jiao et al. (2023) developed a novel pore-scale THMC model considering the coupling phenomena of chemical damage and rock dissolution. The change of fluid pathway due to rock dissolution can be divided into permeation, cavity, and permeation-cavity. The aperture of the fracture remote from the injection point could be larger than that near the injection hole.

Indeed, the variation of reservoir characteristics is a hot topic that favors in-depth knowledge and efficient geothermal development. However, there are rare studies for the quantitative evaluation of different multi-physics effects on geothermal reservoir characteristics variation. In our earlier work (Song G. et al., 2022b), effect ratios were introduced to characterize the interplay between mechanical and chemical effects, as well as poroelasticity and thermoelasticity, to delineate their influence on fracture aperture across both spatial and temporal dimensions. Specifically, using a single THMC model, both chemical aperture and mechanical aperture can be obtained separately, along with poroelastic stress and thermal stress. These ratios could then be determined. Ultimately, the spatial and temporal distributions of these ratios reflect the contributions of mechanical, chemical, thermo-mechanical (TM), and hydro-mechanical (HM) effects. It's worth noting that both mechanical and chemical effects include the MC coupling effects in the above context. MC coupling means that the chemical reaction-induced deformation can cause variations of mechanical deformation (Salimzadeh and Nick, 2019). It has a pronounced impact on reservoir characteristics, particularly on fracture aperture. However, a single fully coupled model cannot distinguish between mechanical and chemical effects and their coupling. As a result, it is difficult to understand how the separate MC coupling, mechanical, and chemical actions influence reservoir characteristics and to comprehend the variation mechanism. The role of MC coupling remained unquantified (Izadi and Elsworth, 2015; Taron and Elsworth, 2009, 2010). Therefore, the concepts of multi-physics action magnitudes were proposed in this work by including five different coupling models: TH, THM, THC, partially THMC, and fully THMC models. Using fracture aperture as the comparison node, set differences among these models are calculated to determine the absolute and relative action magnitudes of separate M, C, and MC coupling.

In section 2, various coupling models—TH, THC, THM, partially coupled THM + C, and fully coupled THMC—are introduced for EGS production. The multi-physics magnitudes of mechanical, chemical, strong MC and weak MC coupling are defined. In section 3, distributions of temperature, pressure, stress, strain, solute concentration, and fracture aperture are presented based on the fully coupled THMC model. Section 4.1 assesses fracture aperture discrepancy among the four coupling models. Sections 4.2 and 4.3 highlight mechanical, chemical, strong MC, and weak MC coupling variations over time and positions. Especially, variations in near-injection well zones and far-injection well zones are presented. Correlative coefficients between multi-physics couplings are provided. Section 4.4 gives an example of how to apply the multi-physics magnitude to analyze the influence of operation strategies (injection solute concentration) on multi-physics effects and production.

2. Model description

2.1. Model assumptions

A reliable multi-physics coupling model is the premise for the analysis of reservoir characteristics. The key critical model assumptions are

made: (1) Formation properties are homogeneous and isotropic (Shi et al., 2019a). (2) Fractures serve as the primary channels for flow, heat transfer, and solute transportation in EGS (Vik et al., 2018). An equivalent fracture aperture is considered. Rock porosity and permeability remain constant. (3) Water is the working fluid. It maintains a fluid state within the temperature and pressure range (20–40 MPa and 100–300 °C). (4) Local thermal equilibrium is assumed, with identical temperatures for rock and fluid (Cao et al., 2016). (5) Amorphous silica is the major chemical reaction mineral in EGS (DiPippo, 2012; Song G. et al., 2022c).

2.2. THMC coupling model

The governing equations of the thermo-hydro-mechanical-chemical coupling model are built considering the fluid flow, heat transfer, mechanical deformation, chemical reaction and solute transportation processes. Fluid flow within the porous and fractured media follows Darcy's law. Heat transfer adheres to Fourier's law. Mechanical deformation is governed by elastic mechanisms, involving displacement and stress as dependent variables (Shi et al., 2019b). The chemical process is mainly controlled by SiO_2-water reactions and Fick's law (Pandey et al., 2015). The fracture aperture is the coupling node, which means all processes are coupled by indirectly or directly changing the fracture aperture (Chen et al., 2018). Comprehensive model equations are presented in Appendix A. The fully coupled THMC model can also be referred to in the published work (Song G. et al., 2022b). The model verifications against simple analytic models were provided as well.

Fig. 2 illustrates the components of the THMC coupling model, encompassing four distinct physical fields and their interconnections. Each physical field corresponds to specific variables, including temperature, pressure, stress, displacement, chemical solution concentration, and fracture aperture. There are seven coupling connections between each two physics fields. They are ① TH (Thermo-Hydro), ② TC (Thermo-Chemical), ③ HC (Hydro-Chemical), ④ TM (Thermo-Mechanical), ⑤ HM (Hydro-Mechanical), ⑥ Strong MC (Mechanical-Chemical) coupling, and ⑦ Weak MC coupling. The above crucial variables are dynamically exchanged in real time within each interrelationship.

The following provides a detailed description of the connections between various physical fields within the geothermal reservoir. **Thermo-hydro (TH) coupling**: Water properties, including viscosity and thermal conductivity, are sensitive to pressure and temperature changes. Consequently, flow resistance is altered accordingly, leading to an impact on thermal convection in turn. **Thermo-mechanical (TM) coupling**: Variations in local temperature from the initial state induce thermal stress and thermoelastic deformation, causing alterations in fracture aperture. **Thermo-chemical (TC) coupling**: The reaction rate constant and equilibrium concentration of chemical reactions are influenced by both temperature and solute concentration. This results in changes in fracture gapping due to chemical dissolution and precipitation. **Hydro-mechanical (HM) coupling**: Variations in water pressure induce changes in effective stress, altering fracture width and permeability, and consequently impacting flow velocity within the fracture system. **Hydro-chemical (HC) coupling**: Water flow within fractures transports solutes. It causes deviations from equilibrium concentration and initiates precipitation and dissolution processes. These processes subsequently alter the chemical aperture and fracture conductivity. **Mechanical-chemical (MC) coupling** can be classified into strong and weak coupling effects. Strong MC coupling involves a direct relationship between two fields. Chemical reaction-induced deformation triggers stress redistribution, altering the mechanical aperture. Weak MC coupling, on the other hand, operates indirectly. Stress-induced deformation modifies fracture aperture and permeability, influencing convective heat transfer, which in turn impacts flow and temperature fields. Fluctuations in temperature and pressure cause variations in reaction concentration transport and chemical reactions, thereby affecting reaction-induced deformation. Conversely, the chemical field indirectly influences stress deformation through the thermal and hydraulic fields. The weak MC coupling entails the interplay between stress and chemical fields indirectly via flow and heat transfer.

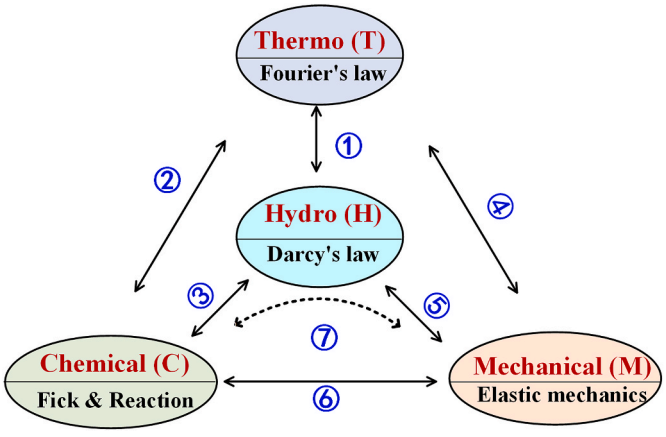

Fig. 2. The coupling among the fluid flow, heat transfer, mechanical deformation and chemical reaction (Song G. et al., 2022b).

Five essential coupling models are established accounting for various scenarios: TH, THC, THM, partially coupled THMC (THM + C), and fully coupled THMC coupling models. They are characterized by distinct combinations of coupling relationships and their corresponding physical fields: The **TH model**, a fundamental geothermal production model, comprises the thermal and hydraulic fields only with the TH coupling relationship. This model primarily examines fluid flow and heat transfer in porous media and fractures. The **THC model** encompasses fluid flow, heat transfer, chemical reactions, and solute transportation within geothermal reservoirs, integrating TH, HC, and TC coupling relationships. Changes in fracture aperture result from chemical dissolution or precipitation of silica minerals. They would play a substantial role in shaping geothermal production characteristics. The **THM Model** includes fluid flow, heat transfer, and mechanical deformation during thermal extraction, encompassing TH, TM, and HM coupling relations. Fracture aperture is influenced by mechanical effects, such as poroelasticity stress and thermoelasticity stress. The partially coupled THMC model is called as **THM + C model** hereinafter. It incorporates all coupling processes except for strong MC coupling. It involves the indirect coupling of chemical and mechanical deformation effects. The fully coupled **THMC model** integrates all essential physical fields, encompassing TH, TM, TC, HM, HC, and MC couplings. Notably, chemical deformation leads to stress and deformation redistribution within the reservoir.

2.3. Multi-physics strength

Different multi-physics coupling models involve various physical fields and their coupling relationships. The principle of multi-physics coupling intensity calculation is illustrated in Fig. 2. The TH coupling model only contains the coupling relationship ①, whereas the THC coupling model includes coupling relationships ①, ②, and ③. Therefore, the chemical field is considered to be influenced by the combined effects of ② and ③ which constitute the chemical effect. The THM coupling model includes coupling relationships ①, ④, and ⑤. Hence, the mechanical effect is attributed to the combined effects of ④ and ⑤. The THM + C partially coupled model does not include the strong MC coupling effect ⑥. It encompasses the coupling relationships ①, ②, ③, ④, ⑤ and ⑦. The THMC fully coupled model includes all coupling relationships, namely, ①, ②, ③, ④, ⑤, ⑥ and ⑦. By employing the control variable method, the set difference of variables are obtained across different multi-physics coupling models. The impacts of the

mechanical field (M), chemical field (C), and mechanical-chemical coupling (MC) on the fracture aperture are quantitatively calculated. The formula for calculating the absolute strength of each effect is as follows (Iooss and Lemaître, 2015; Pianosi et al., 2015):

$$AS_{\mathrm{M}} = d_{\mathrm{THM}} - d_{\mathrm{TH}} \tag{1}$$

$$AS_{\mathrm{C}} = d_{\mathrm{THC}} - d_{\mathrm{TH}} \tag{2}$$

$$AS_{\mathrm{SMC}} = d_{\mathrm{THMC}} - d_{\mathrm{THM+C}} \tag{3}$$

$$AS_{\mathrm{WMC}} = d_{\mathrm{THM+C}} - d_{\mathrm{TH}} - S_{\mathrm{M}} - S_{\mathrm{C}} \tag{4}$$

where d is an alternative variable like temperature, pressure, fracture aperture, etc. In this research, d represents the fracture aperture. It can be the average aperture of the fracture surface or the aperture at a specific point. AS_{M}, AS_{C}, AS_{SMC}, and AS_{WMC} represent the absolute strength of the mechanical effect, chemical effect, strong MC coupling, and weak MC coupling effect, respectively. By normalizing these four values, the corresponding relative strength of the effect RS is obtained (Iooss and Lemaître, 2015; Pianosi et al., 2015):

$$RS_{\mathrm{M}} = \frac{|AS_{\mathrm{M}}|}{|AS_{\mathrm{M}}| + |AS_{\mathrm{C}}| + |AS_{\mathrm{SMC}}| + |AS_{\mathrm{WMC}}|} \times 100\% \tag{5}$$

$$RS_{\mathrm{C}} = \frac{|AS_{\mathrm{C}}|}{|AS_{\mathrm{M}}| + |AS_{\mathrm{C}}| + |AS_{\mathrm{SMC}}| + |AS_{\mathrm{WMC}}|} \times 100\% \tag{6}$$

$$RS_{\mathrm{SMC}} = \frac{|AS_{\mathrm{SMC}}|}{|AS_{\mathrm{M}}| + |AS_{\mathrm{C}}| + |AS_{\mathrm{SMC}}| + |AS_{\mathrm{WMC}}|} \times 100\% \tag{7}$$

$$RS_{\mathrm{WMC}} = \frac{|AS_{\mathrm{WMC}}|}{|AS_{\mathrm{M}}| + |AS_{\mathrm{C}}| + |AS_{\mathrm{SMC}}| + |AS_{\mathrm{WMC}}|} \times 100\% \tag{8}$$

Song G. et al. (2022b) introduced ratios of mechanical to chemical effects and poroelasticity to thermoelasticity as indicators of multi-physics coupling degrees. They are determined through fracture and stress ratios with a single THMC fully coupled model. However, the proposed calculation method presented here not only elucidates the influence of mechanical and chemical fields but also specifically highlights the impact of mechanical-chemical coupling on fracture characteristics. This facilitates the evaluation of the relative significance of distinct physical fields and their correlations.

3. Model solution

3.1. Geometric model

Artificial hydraulic fracturing is employed to construct EGS (McClure and Horne, 2014). Fracture networks are created with artificial fractures for the construction of the stimulated reservoir volume (SRV) (Song et al., 2018). This enhances reservoir permeability which is easy for flow and heat transfer. An ideal three-well EGS model is established based on previous data as presented in Fig. 3 (Song G. et al., 2022c). A detailed description can be found in previous research publications (Shi et al., 2019b; Song G. et al., 2022c). It mainly comprises surrounding rock, SRV, fractures, one injection well, and two production wells. Low-temperature water is injected from the designated point, extracting heat and flowing to two production points. Table 1 shows the properties of SRV and fracture.

Fig. 4 presents key points on natural fracture surface F at a depth of 3400m. These points are useful in analyzing variations in fracture aperture and multi-physics degree. Point I is the injection site (500 m, 500 m), while P_1 (300 m, 500 m) and P_2 (800 m, 500 m) are the production points. The line P_1P_2 defines the inter-well connection on fracture F. Points A and B represent intervals between injection and production wells. Points D and E are positioned on either side of the production well. Point D is on the side closer to the injection well,

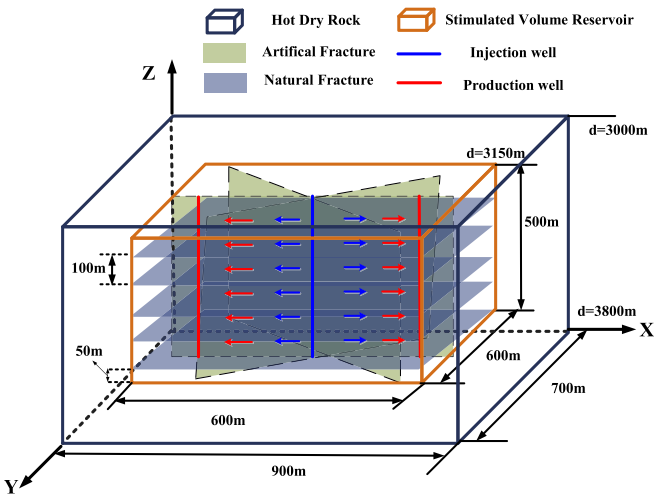

Fig. 3. The geometric diagram of the triple well fractured EGS (Song G. et al., 2022a).

Table 1
Properties for EGS reservoir (Lei et al., 2020; SONG et al., 2021).

Properties	SRV	Fracture
Porosity	0.0354	1
Permeability	0.5 mD	50 D
Density	2607 kg/m^3	2000 kg/m^3
Heat capacity	754.4 J/(kg·K)	750 J/(kg·K)
Thermal conductivity	2.51 W/(m·K)	2.5 W/(m·K)
Storage coefficient	5×10^{-10} 1/Pa	10^{-10} 1/Pa
Thermal expansion coefficient	5×10^{-6} K^{-1}	5×10^{-6} K^{-1}
Biot-Willis coefficient	0.7	0.7
Young's modulus	44.1 GPa	44.1 GPa
Poisson' ratio	0.23	0.23
Silica mass content	70%	/
Mole number of silicas per unit mass of rock	23.3 mol/kg	/
Solute diffusion coefficient	10^{-9} m^2/s	10^{-9} m^2/s
Coefficient of fracture irregularity	/	0.5
Fracture normal stiffness	/	1200 GPa/m

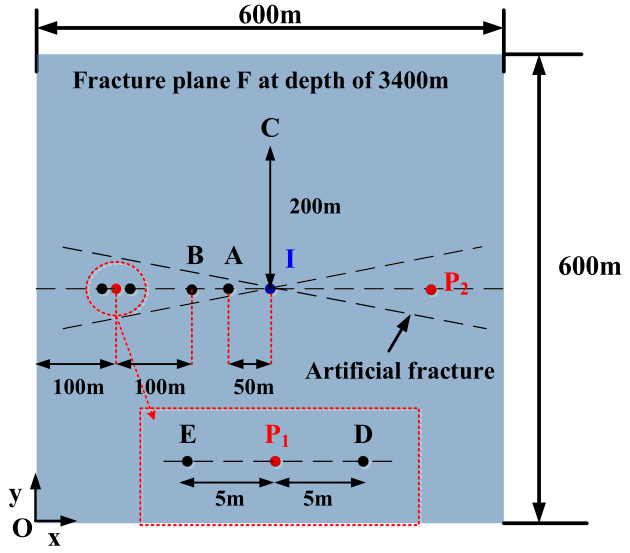

Fig. 4. The distribution of typical points at the middle fracture plane F.

defined as the strong side, while point E is situated closer to the boundary, defined as the weak side. Point C illustrates the reservoir variations in the remote well zone. The non-uniform aperture distribution on fracture plane F is also investigated.

3.2. Initial and boundary conditions

Table 2 presents the initial and boundary conditions adopted for geothermal production. For the temperature distribution, the top of the geometric model at 3000 m has a 200 °C temperature with a 0.05 °C/m gradient. The bottom well temperature is around 200 °C. Adiabatic heat flux applies to four peripheral boundaries. The top and bottom are fixed temperature boundaries that match the initial temperature. Pressure at 3000 m is 30 MPa with a 5000 Pa/m gradient. Adiabatic flow flux boundaries encompass the HDR. The mechanical field considers initial stress equilibrium. The study focuses on relative stress changes due to temperature and fluid pressure variations. Hot dry rock boundaries are supported with zero normal displacements. For component transportation, the initial concentration is in equilibrium. Silica is the main reactive mineral. The initial average equilibrium concentration is 0.0173 mol/kg according to equation (29) in Appendix A. For underbalanced injection, the injection concentration at the well is 0 mol/kg. For overbalanced injection, the injection concentration at the well is 0.025 mol/kg. Adiabatic component flux boundaries enclose the reservoir. The line element identifies the well in the model. Fractures start with a geometric aperture of 0.5 mm and a hydraulic aperture of 2.45 × 10^{-5} mm. The working fluid is injected at a stable injection rate of 40 kg/s and an injection temperature of 60 °C. It is produced at a fixed pressure of 30 MPa. A 30-year EGS production is simulated as the above parameters.

3.3. Model calculation

In this study, COMSOL Multiphysics is utilized to compute the THMC coupling process for geothermal production simulation based on the finite element method (Cristea et al., 2010; Li et al., 2009; Multiphysics, 2017). Five modules are employed for the computation. Darcy's law module is utilized to solve flow processes in porous media. Within this module, fracture flow nodes are set up to solve flow processes within fractures. Well nodes are used to represent injection and production wells. The porous media heat transfer module is used to solve heat transfer within the bedrock. Fracture nodes are chosen to solve heat transfer within fractures, employing a line heat source boundary to represent injection heat sources. The solid mechanics module is employed to solve stress and deformation processes in the reservoir. A thin elastic layer is used to describe changes in fracture aperture under varying stress conditions. The porous media mass transfer module addresses component transport within the bedrock. Fracture nodes are selected to solve component transport within fractures, with component source terms defined from chemical reaction processes. A line mass source is used to describe solute injection boundaries. The boundary ordinary differential equation module is utilized to customarily solve the evolution process of fracture aperture caused by chemical reaction. Multiple coupling relationships like porous elasticity and thermal expansion are also included. Key physical variables can be transferred in real-time.

Fig. 5 illustrates the computational process of the thermo-hydro-mechanical-chemical coupling model. Symbol i is ith time step and j denotes the jth iteration step. K means the coefficient matrix for the respective equation group and b is the nonlinear source function. Variables of p, T, c, u, v, w, and d identify the pressure, temperature solute concentration, displacements in x, y, and z directions, and fracture aperture. A segregated solver is employed to solve the coupling variables within a time step. The following physical equations are sequentially computed: flow equation, heat transfer equation, component transport equation, fracture aperture differential equation and solid mechanics equation at time t_i. Each step utilizes solutions from the previous steps. The flow equations provide pressure X_p for the heat transfer part. For solute transportation questions, variables of pressure X_p and temperature X_T are used for the calculation. The same variable transfer approach can be applied to Steps 4 and 5. Newton-Raphson iteration continues until the convergence of nonlinear problems. The convergence criterion for any dependent variable is set as a maximum relative tolerance of 10^{-4}. The back-differential method is utilized for transient problems. A total of 120 000 meshes are adopted considering both calculation cost and error control. The meshes in the SRV region, as the main field for flow and heat transfer, are extremely fine. The detailed mesh regime can

Table 2
Parameters of the initial conditions for the numerical case (Song G. et al., 2022b).

Parameters	Values
Pressure at 3000m subsurface	30 MPa
Pressure gradient	5000 Pa/m
Injection rate	40 kg/s
Production pressure	33 MPa
Temperature at 3000m subsurface	200 °C
Temperature gradient	0.05 °C/m
Injection temperature	60 °C
Initial concentration	equilibrium at the initial temperature
Injection concentration	0 mol/kg for undersaturation 0.025 mol/kg for oversaturation
Real equivalent Aperture	0.5 mm
Initial Hydraulic aperture	2.45 × 10^{-5} mm

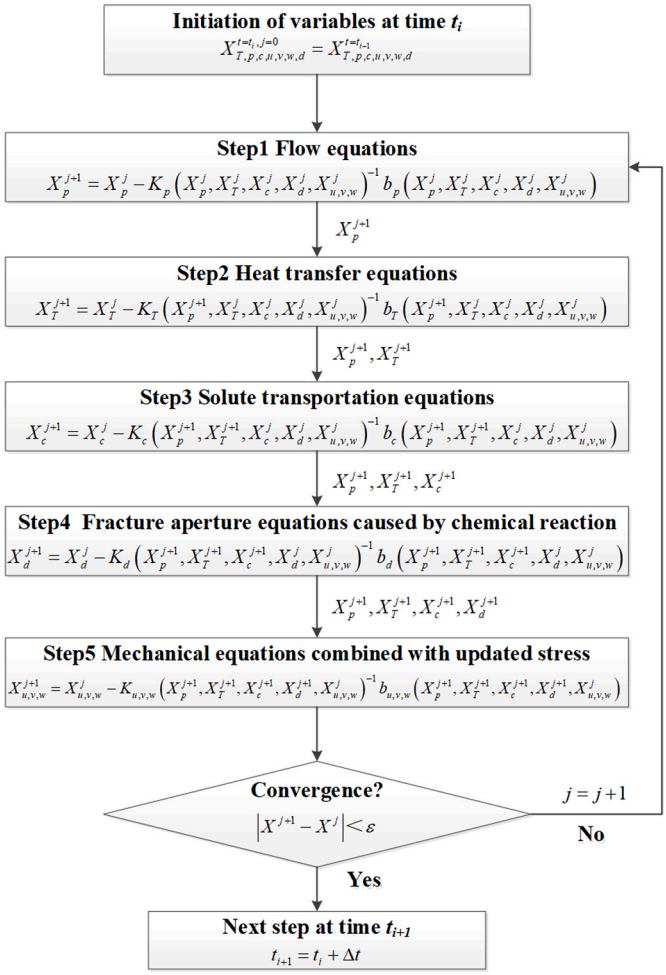

Fig. 5. Segregated method calculation process for THMC fully coupled models.

be referenced in the published paper (Song G. et al., 2022a) where mesh independence analysis is conducted.

3.4. Multi-physics distribution in EGS

Key characteristics examined encompass temperature, pressure, stress, strain, and solute concentration.

3.4.1. Temperature

Fig. 6 depicts temperature distributions throughout EGS production at intervals of 1, 5, 10, and 20 years. The color scale ranges from blue (low temperature) to red (high temperature), with the minimum temperature matching the injection temperature of 60 °C. The low-temperature region, resembling a cylinder, emanates from the injection wells and progressively extends toward the production wells. The low-temperature area has reached the production points after 3 years as shown in Fig. 7. Fractures serve as the main channels for thermal breakthrough.

3.4.2. Pressure

Figs. 8 and 9 illustrate the pressure distribution in reservoir and along the inter-well line P_1P_2 throughout EGS production respectively. The high-pressure region centers around the injection well, while a low-pressure area surrounds the production well. Pressure increases with depth, forming a cone-shaped high-pressure zone that expands over time. After 20 years, the maximum pressure reaches 45.6 MPa which occurs at the well bottom in Fig. 8. An arrow denotes flow direction and velocity, indicating water movement from the injection well to the production well.

3.4.3. Stress and strain

Fig. 10 illustrates the Mises stress (Shi et al., 2019b) distribution in the reservoir over 1, 5, 10, and 20 years. Initially, the area near the injection well experiences heightened stresses, reaching a peak Mises stress of 32.4 MPa. There is a notable temperature gradient near the injection well that induces significant thermal stresses. As production advances, this high-stress zone gradually extends towards the production well, accompanied by declining Mises stress values. The expansion of the low-temperature region and the diminishing temperature gradient contribute to stress reduction. Moreover, chemical deformation triggers spatial stress redistribution (Song G. et al., 2022b), further decreasing Mises stress. In reality, the diffusion of the high-stress area correlates with the diffusion of the low-temperature region. Fractures represent low-stress regions, contrasting with the high-stress conditions of the surrounding bedrock. Fractures experience low-temperature and low-pressure states, while the bedrock encounters high-temperature and high-pressure conditions.

Fig. 11 illustrates volumetric strain distribution maps within the geothermal system. They are similar to temperature distribution patterns. Deformation is most pronounced near the injection well and gradually extends toward the production well. At the fractures-geothermal reservoir intersection, notable strains arise due to rapid fluid propagation through fractures. Fig. 12 depicts volumetric strain distribution along the P_1P_2 connection between injection and production wells. Generally, strain is negative and the value increases with time. It displays a "W" shape along P_1P_2. Deformations near the injection well are greater, peaking and then diminishing towards the production wells. These behaviors arise from the combined influences of effective stress, thermal stress and chemical effects.

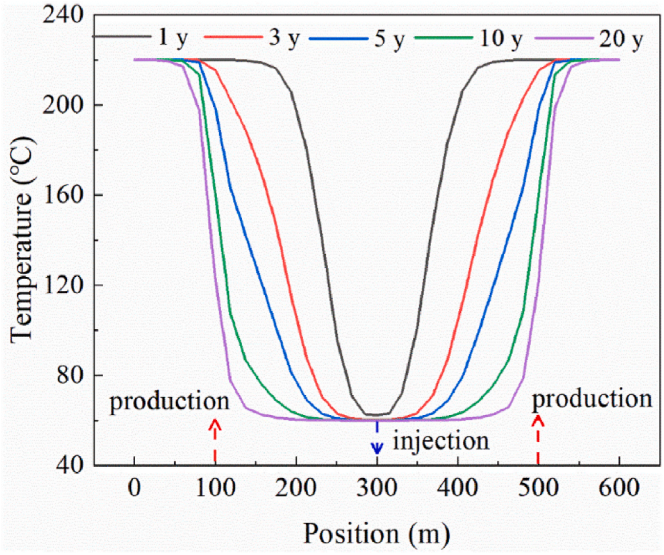

Fig. 7. Temperature distribution along the line P_1P_2 between wells after 1, 3, 5, 10 and 20 years.

3.4.4. Solute concentration

Fig. 13 depicts the spatial distribution of solute concentration following underbalanced injection (0 mol/m^3). The low-concentration solute gradually diffuses from the injection well to the production well. The low-concentration region is more extensive than the low-temperature area within the same production timeframe. By the 20-year mark, it occupies nearly the entire reservoir space. Fig. 14 displays concentration distribution curves along the line P_1P_2. These curves assume a concave shape, with the low-concentration solute already diffusing to the production well after just 1 year. This highlights the higher sensitivity of solute convection compared to heat convection.

3.4.5. Fracture aperture

Fig. 15 shows the contour maps of fracture aperture distribution on plane F over 1, 5, 10, and 20 years of geothermal reservoir production. The high fracture aperture is highlighted in red. It forms an elliptical distribution pattern with the injection well at the center. This pattern is closely related to the low-temperature area's shape. The red area expands over time, accompanied by progressive fracture aperture enlargement. The maximum fracture aperture attains 0.53 mm after 20 years. Fig. 16 shows the distribution curves of the fracture aperture along the line P_1P_2. The maximum aperture is observed near the injection well and rapidly decreases towards the production well. It is attributed to the steep increase in fluid pressure and significant temperature decrease near the injection well, and sharp pressure drop near

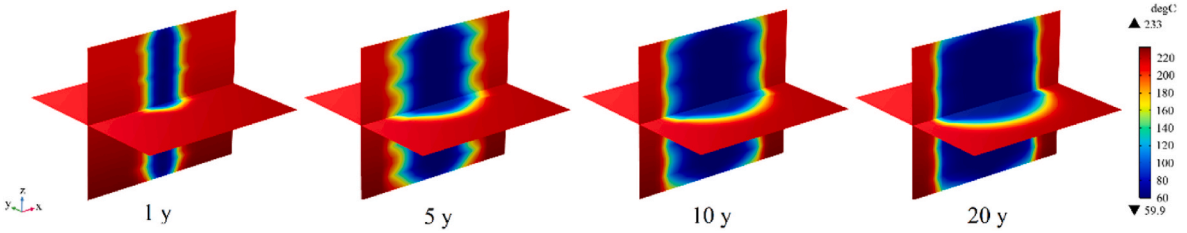

Fig. 6. Reservoir temperature distribution after 1, 5, 10 and 20 years.

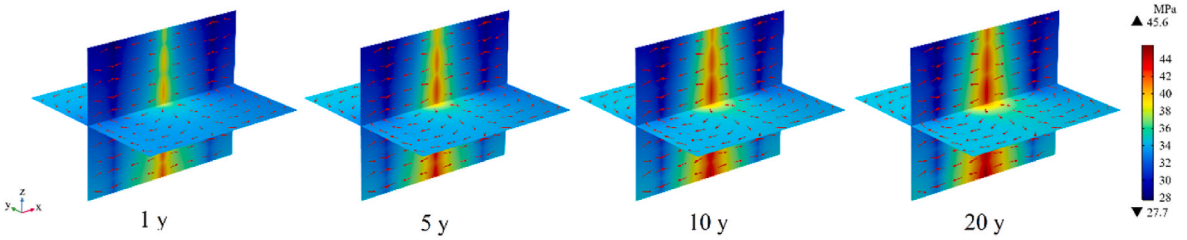

Fig. 8. Reservoir pressure distribution after 1, 5, 10 and 20 years.

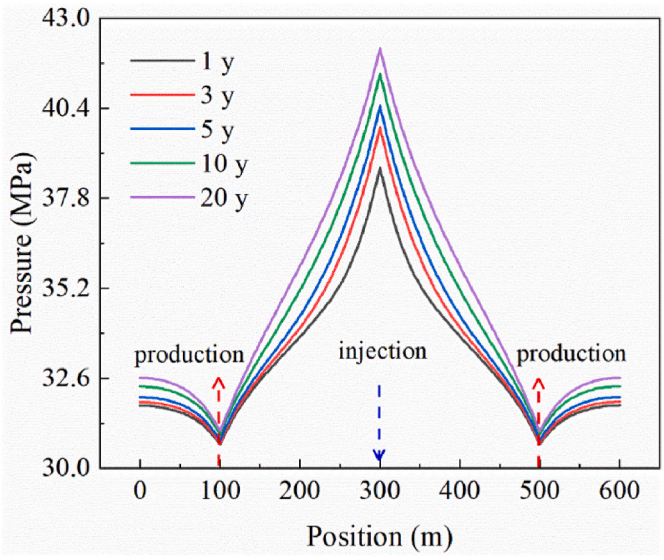

Fig. 9. Pressure distribution along the line P_1P_2 between wells after 1, 3, 5, 10 and 20 years.

the production well. With ongoing exploitation, the aperture difference between the injection and production well regions becomes more distinct. The curve gradually evolves into an "M" shape. The variation exhibits a slow increase followed by a rapid decrease from the injection well toward the production well. This can be explained by the annular distribution of chemical reaction rates as indicated by relevant chemical field variables (Chen et al., 2018; Song G. et al., 2022a). Fracture aperture is primarily influenced by both mechanical and chemical effects.

4. Results and discussions

4.1. Comparison of the fracture aperture among different coupling models

In this section, the indicator of fracture aperture is selected as the calculation basis of multi-physical effect magnitude for the following reasons: a) The evolution of fracture aperture leads to changes in permeability, followed by alterations in flow, convective heat transfer, mass transfer, and stress. It is the fundamental reason for variations in heat extraction. b) Other production indicators of heat extraction, such as temperature, pressure differential, net heat power, power generation, and recovery rate, are indirect consequences of the evolution of fracture permeability. They couldn't be regarded as reservoir features. c) Fracture aperture serves as a direct indicator to differentiate the degree of chemical and mechanical effects, as demonstrated in equation (34). The aperture resulting from chemical effects is referred to as a "chemical aperture," while the one induced by mechanical effects is termed a "mechanical aperture." d) The spatial distribution of fracture aperture illustrates the non-uniformity of the geothermal reservoir's characteristics under multi-physics coupling effects. Therefore, fracture aperture hereinafter is employed as the main indicator.

Fig. 17 shows the distribution of fracture aperture on plane F for THC, THM, THM + C, and THMC coupling models with underbalanced injection after 5 years. Similarly, red zones indicate a high fracture aperture. As for the THC model, there occurs chemical dissolution that causes the increase of fracture aperture. The red zone shows a circle shape which means its value increases and then decreases from injection

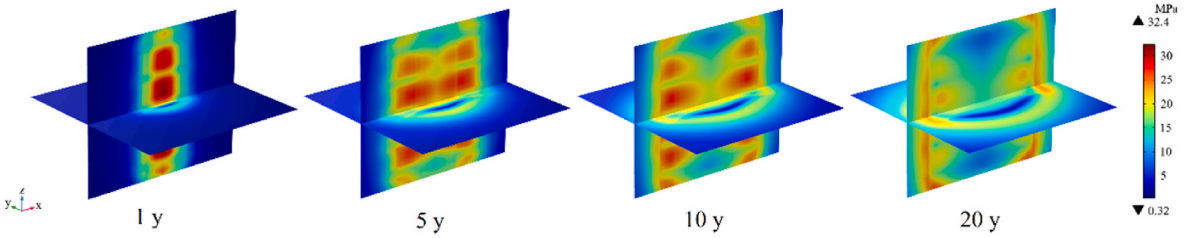

Fig. 10. Reservoir Mises stress distribution after 1, 5, 10 and 20 years.

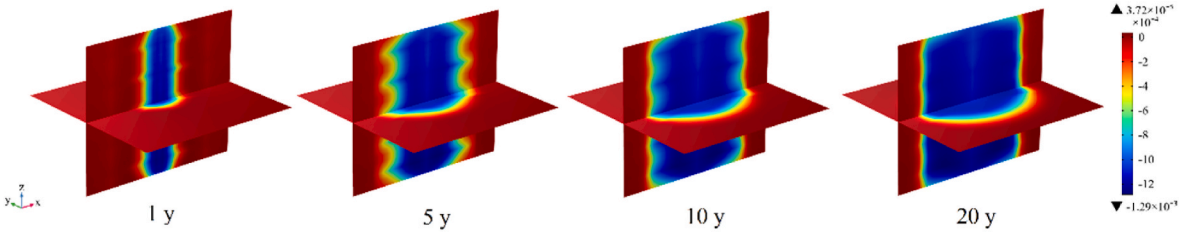

Fig. 11. Reservoir volumetric strain distribution after 1, 5, 10 and 20 years.

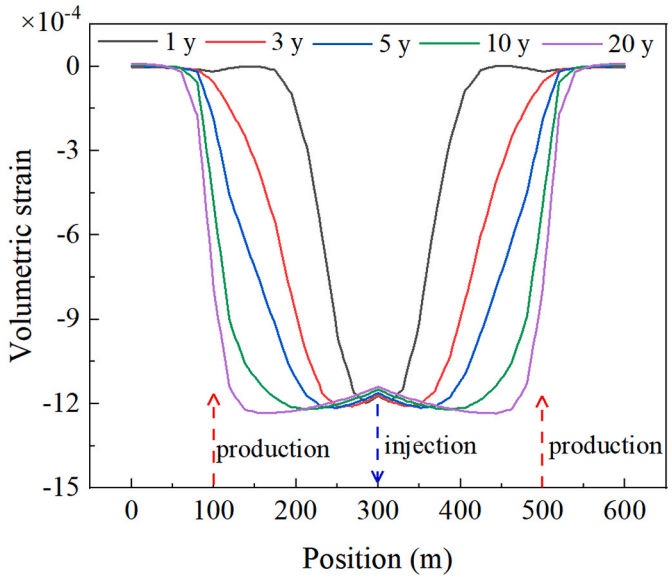

Fig. 12. Volumetric strain distribution along the connection line P_1P_2 between wells.

points to the boundary. It is determined by the chemical reaction rate. This phenomenon shows great agreement with previous work (Pandey et al., 2015). As for the THM model, the red zone is controlled by mechanical effects like efficient stress and thermal stress. For the THM + C partially coupled model, fracture aperture distribution results from the simple summation of THM and THC without constraints between mechanical and chemical behaviors. In the THMC fully coupled model, the fracture aperture shape closely resembles the THM case due to MC coupling. Thus, there is a big difference among different coupling models. Take the average aperture value of fracture F of different models and quantify its variation as Fig. 18. When underbalanced injection, the fracture aperture increases except for the TH model. The THMC fully coupled model aligns closely with THM due to MC coupling effects. THC and THM + C exhibit more pronounced aperture value increases. This kind of difference is the reference basis for the calculation of multi-physics strength.

4.2. Magnitude of multi-physics effects

To explore the comprehensive action strength of different coupling effects, the absolute multi-physics degree is determined by equations (1)–(4) with the average aperture of fracture F. Fig. 19 illustrates the variations in the absolute intensity of mechanical, chemical, strong MC, and weak MC coupling. With the undersaturated injection conditions, chemical strength exhibits a positive trend with a gradual increase. The chemical effect improves fracture aperture. This enhancement correlates with the reservoir's underbalanced state which induces dissolution reactions. Nonetheless, the extent depends on the chemical reaction degree. There shall be potential differences under balanced and overbalanced injection conditions. It is necessary to investigate outcomes from different injection concentrations. Mechanical absolute strength displays a progressive increase, driven by mechanical effects that enhance fracture aperture. However, its influence is notably lower than the chemical effect, indicating that mechanical effects like thermoelasticity and poroelasticity are less evident than the chemical reaction in this paper's undersaturation context. Conversely, strong MC coupling exhibits negative values with increasing absolute magnitude, reflecting a reduction in fracture aperture. This result emerges from chemical effects triggering mechanical stress redistribution. Regarding weak MC coupling strength, it remains slightly above 0, indicating a minor role in fracture variation under undersaturated injection. However, it remains a crucial element of the overall MC coupling and should not be overlooked.

To quantify the contribution percentage of various multi-physics factors to the variation in fracture aperture during different production periods, Fig. 20 displays the relative strength of different effects at 0.3, 0.5, 5, and 10 years. At an early stage of production (0.3 years), the mechanical effect accounts for 46.91% of the variation in fracture aperture. This underscores the controlling influence of mechanical effects at the onset of geothermal production. This finding highlights the need to consider reservoir damage from stress during the early production phase. Over time, the strong MC coupling and chemical effects gradually assume more control over the overall variation in fracture aperture. After 10 years, the two effects contribute 47.64% and 48.02% respectively, whereas the mechanical effect's contribution diminishes to 4.03%. This shift underscores the increasing significance of chemical and MC coupling effects. Thus, it is necessary to consider chemical-induced precipitation and scaling in later production stages.

The multi-physics effect not only exhibits temporal variation but also spatial variation. Fig. 21 shows the variation of multi-physics degrees at

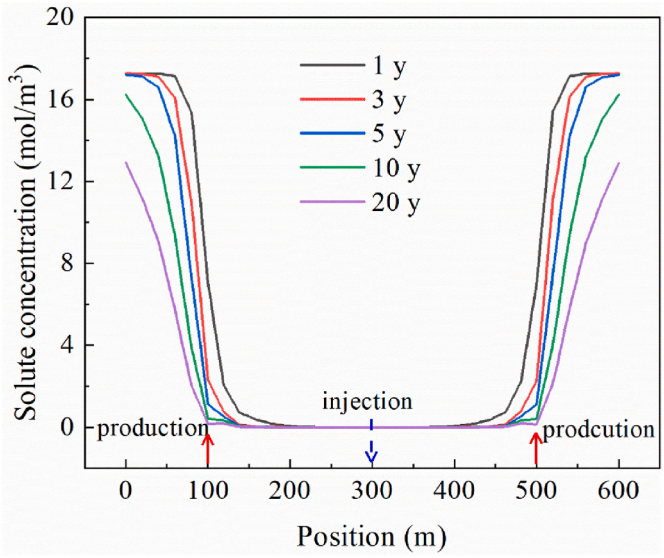

Fig. 14. Solute concentration distribution along the connection line P_1P_2 between wells.

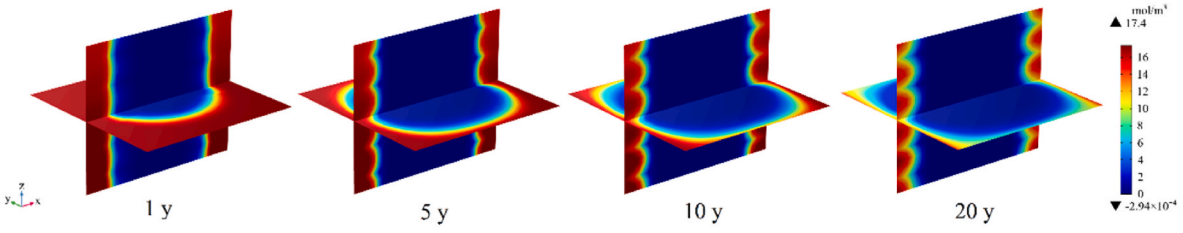

Fig. 13. Reservoir solute concentration distribution after 1, 5, 10 and 20 years.

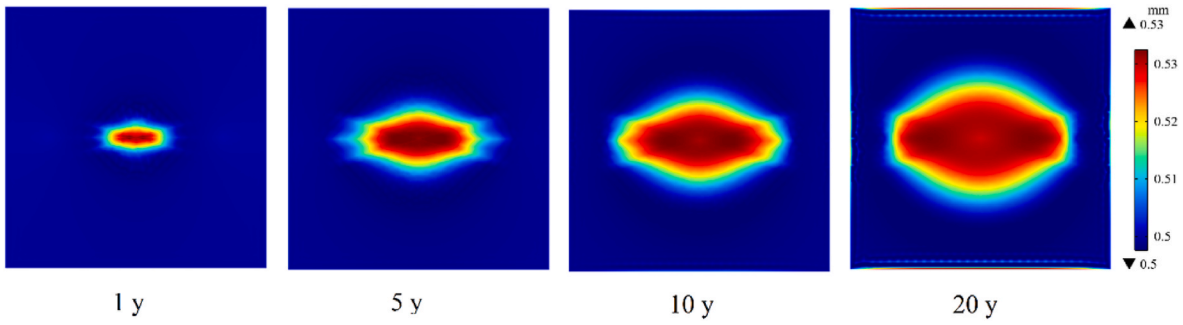

Fig. 15. Fracture aperture distribution of F after 1, 5, 10 and 20 years.

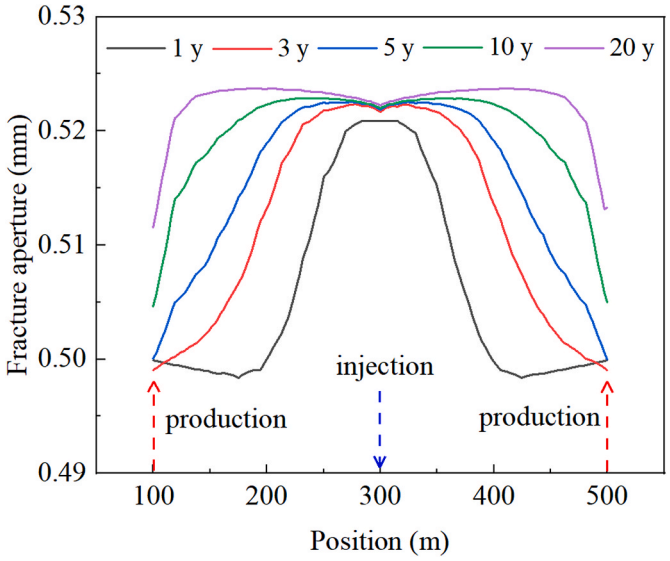

Fig. 16. Fracture aperture distribution along the connection line P_1P_2 between wells.

point B which is at the midpoint between the injection and production well. The degree of mechanical effect exceeds 0, gradually increasing and then slowly decreasing. This pattern signifies that effective stress and thermal stress bolster the fracture aperture at this position. Similarly, the chemical effect rises gradually and then stabilizes which indicates chemical dissolution enhancing the fracture aperture. In contrast, the strong MC coupling degree is negative and can cause the reduction of the aperture at this position. It presents an opposing trend to the chemical effect. Meanwhile, the weak MC coupling effect slightly exceeds 0, modestly enhancing the fracture aperture. During stable production at position B, the absolute strength of M is notably higher than other effects. C and strong MC coupling effects exhibit near-equal absolute strengths with opposite effects. The former augments the fracture aperture whereas the latter effect diminishes it. The absolute strength of weak MC is marginally above 0. Furthermore, Fig. 21 displays the relative strength of the multi-physics effects on the variation of fracture characteristics after 15 years. The relative strengths of M, C, strong MC, and weak MC are 62.89%, 18.54%, 18.42%, and 0.15%, respectively. This observation highlights that mechanical stress holds sway over reservoir characteristics at point B during stable production.

To assess the interplay among the four multi-physics strengths, Table 3 lists the correlation coefficient of them for point A. Remarkably, the correlation coefficient between strong MC and C reaches an impressive −0.97. The relationship between strong MC and M yields a correlation coefficient of −0.77. These results signify strong negative correlations at the midpoint position of A. It is inferred that different positions exhibit distinct correlation patterns. To provide a comprehensive perspective, correlation coefficients among the four effects are computed at typical points B, C, and D individually. Table 4 presents the average correlation coefficient among four effects. The value between strong MC and C is −0.93452 while other coefficients are closer to 0. It is deduced that C triggers strong MC indeed and chemical reactions induce stress redistribution.

4.3. Multi-physics effects at different positions

Five distinct points, labeled as A, B, C, D, and E as demonstrated in Fig. 4, are strategically selected to assess the evolution of the absolute strengths of the multi-physics effects M, C, strong MC, and weak MC coupling. Fig. 22(a) shows the variations of the absolute mechanical strength. It is larger between the injection and production wells resulting from the combined effect of effective stress and thermal stress between wells. The closer to the injection wells, the higher the rise rate of the mechanical effect. Conversely, the absolute strength of M in the weak domain of the production well and the remote well region assumes a relatively diminished state. This phenomenon is attributed to the low values of effective stress and thermal stress. Correspondingly, Fig. 22(b) delineates the variations of the absolute chemical strength across different designated points. The magnitude of the chemical effect first

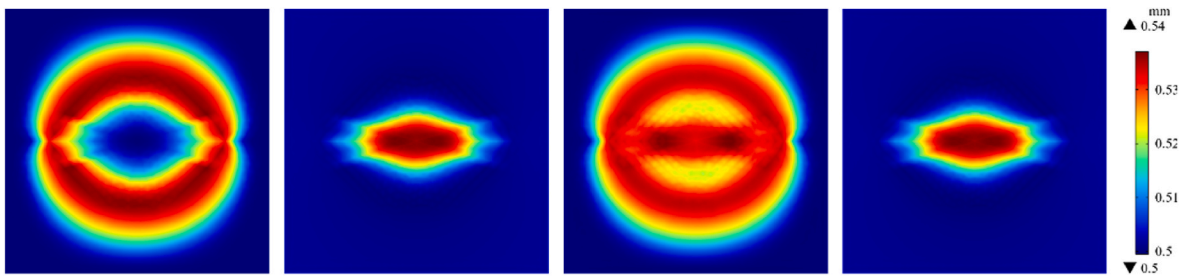

Fig. 17. Fracture aperture distributions of fracture F after 5 years under TH, THM, THM + C and THMC models (left to right).

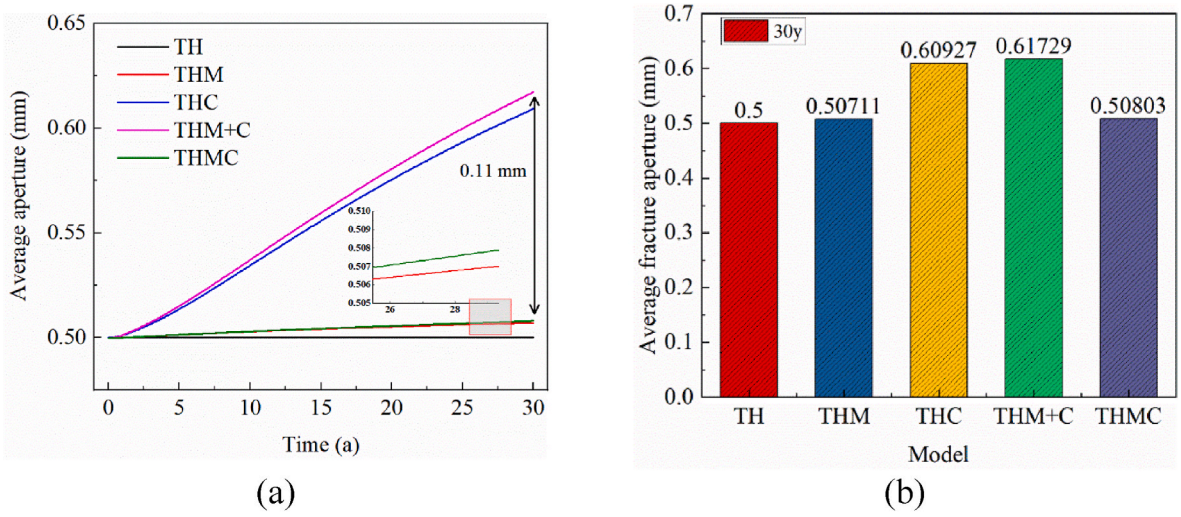

Fig. 18. Average fracture aperture of plane F for different coupling models: (a) variation with time; (b) average value on 30th year.

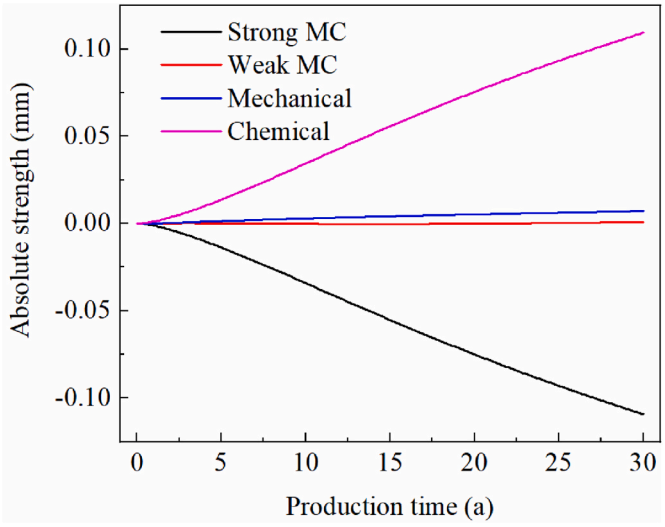

Fig. 19. The overall magnitude variation of mechanical, chemical, strong MC coupling and weak MC coupling during EGS production.

increases and then gradually levels off between the injection and production wells. The closer to the injection well, the lower the chemical effect due to the lower temperature, where chemical reactions hardly occur. The strength of the chemical field gradually intensifies on the weak side of the production well and in the far well region. Chemical reactions are more active in these locations due to the high temperature and unbalanced chemical concentration. These significantly alter the aperture of fractures. Therefore, it is conceivable to discern the mechanical-dominant zone and the chemical-dominant zones. The former region aligns between the injection and production wells, whereas the latter zone is primarily situated within the remote well domain and the weak side of the production well vicinity.

The pie diagrams Fig. 23 are drawn to represent the relative strengths of different coupling effects for the near-well point A and far-well point C after 15 years. The relative strength of the mechanical effect in the near-well region is 81.74%, indicating that the mechanical effect dominates in this area which is the mechanical-dominant zone. In contrast, the relative strength of the chemical field in the far-well region is 48.23%, indicating that the chemical effect dominates in this region which is a chemical-dominant zone.

The preceding observations are compared with findings from prior research employing the proportion method to evaluate contributions of poroelasticity, thermoelasticity, and chemical effects (Song G. et al., 2022b). The results are illustrated through the contour map distribution for fracture F in Fig. 24. The evolution of fracture aperture from the injection well towards boundaries is sequentially influenced by poroelasticity, chemical, and thermoelasticity effects. Poroelasticity, governed by effective stress, predominantly manifests at boundaries. It is prominent initially and then gradually weakened. Thermoelasticity, subjected to temperature variation, prevails between injection and production wells. It is coinciding with low-temperature regions and expanding increasingly. The area of chemical effect surrounds the thermoelasticity-dominant zone, particularly evident at points of temperature discontinuity where chemical reaction rates shift abruptly. The chemical effect initially contributes modestly but its influence gradually escalates over time. Two prevailing zones emerge when stable production: the mechanical-dominant area, situated between injection and production wells, and the chemical-dominant domain, localized in the distant well region. Consequently, consistent conclusions are obtained from different computational methodologies–previous proportion method and the proposed multi-physics strength approach.

Recommendations can be provided according to the above results. For instance, operational strategies can be implemented during the initial stage around the injection wells. Employing high-temperature and low-pressure injection can mitigate mechanical damage in the vicinity of injection wells, helping to reduce the possibility of fault activation and seismic risks. The use of water jet technology (Li et al., 2010) is also effective for removing blockages and increasing permeability near injection wells. In the later stages of production, chemical clogging may become a concern around the production well. Utilizing swirling water jet technology (Zhang et al., 2023) can effectively remove scaling in the wellbore. High-pressure water jet applications can also help reduce clogging near production wells. In cases of severe scaling, a potential solution is to convert production wells into injection wells. This approach allows the original chemical-driven areas to gradually transition into mechanical-driven areas.

4.4. *Influence of chemical injection solute concentration*

To further visually elucidate the meaning of multi-physics coupling effects, Figs. 25 and 26 present the influence of chemical injection solute concentrations on the magnitudes of M, C, strong MC, and weak MC coupling effects. Here, the solute concentration denotes the SiO_2 content in the working fluid. The balanced injection concentration equals

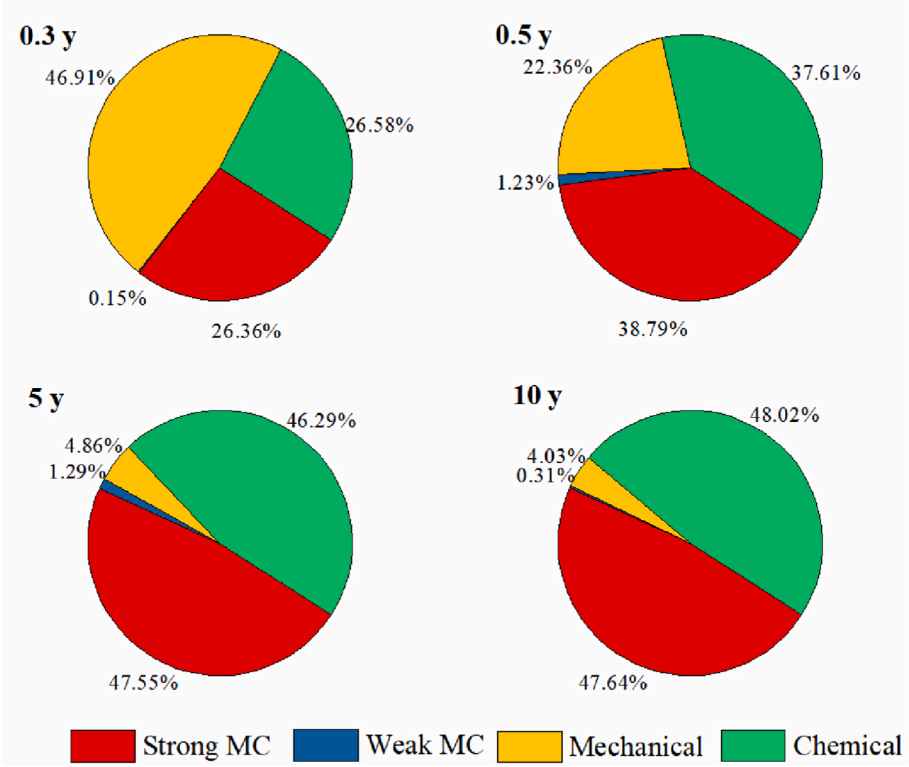

Fig. 20. Relative magnitude of mechanical, chemical, strong MC coupling and weak MC coupling over 0.3, 0.5, 5 and 10 years.

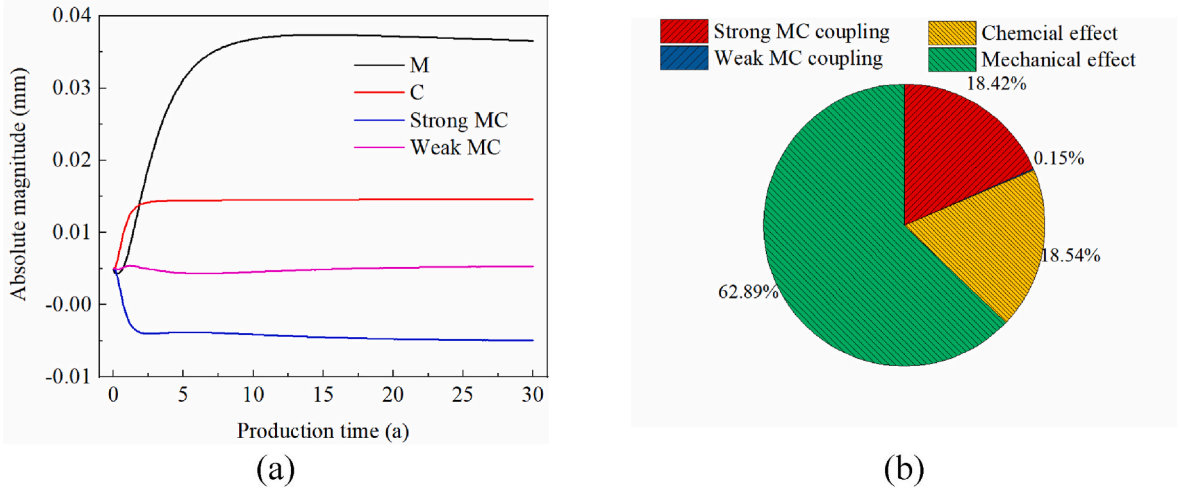

Fig. 21. Point B between injection and production wells: (a) variations of absolute strength with time; (b) the relative strength after 15 years.

Table 3
Correlation of M, C, strong MC and weak MC coupling strength for point B.

Correlative coefficients	Strong MC coupling	Weak MC coupling	Chemical (C) effect	Mechanical (M) effect
Strong MC coupling	1	−0.1712	−0.97085	−0.77016
Weak MC coupling	−0.1712	1	−0.06484	−0.0568
Chemical (C) effect	−0.97085	−0.06484	1	0.763632
Mechanical (M) effect	−0.77016	−0.0568	0.763632	1

Table 4
Average correlative coefficients of M, C, strong MC coupling and weak MC coupling strength.

Correlative coefficients	Strong MC coupling	Weak MC coupling	Chemical (C) effect	Mechanical (M) effect
Strong MC coupling	1	−0.22824	−0.93452	−0.27011
Weak MC coupling	−0.22824	1	0.063298	0.076763
Chemical (C) effect	−0.93452	0.063298	1	0.337486
Mechanical (M) effect	−0.27011	0.076763	0.337486	1

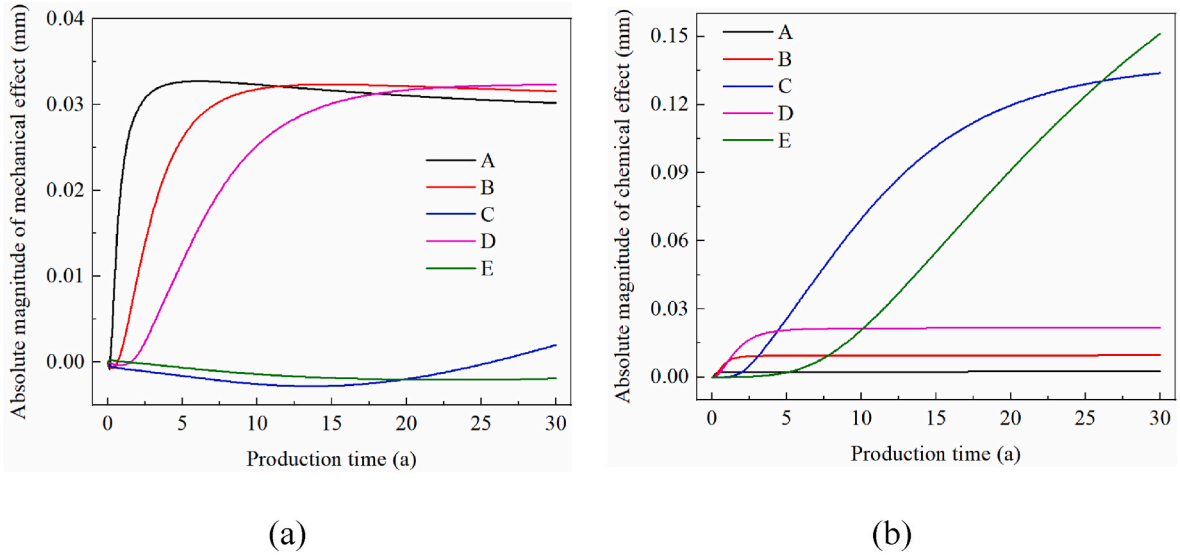

Fig. 22. Variations of physical field absolute strength with time at A, B, C, D and E: (a) mechanical field; (b) chemical field.

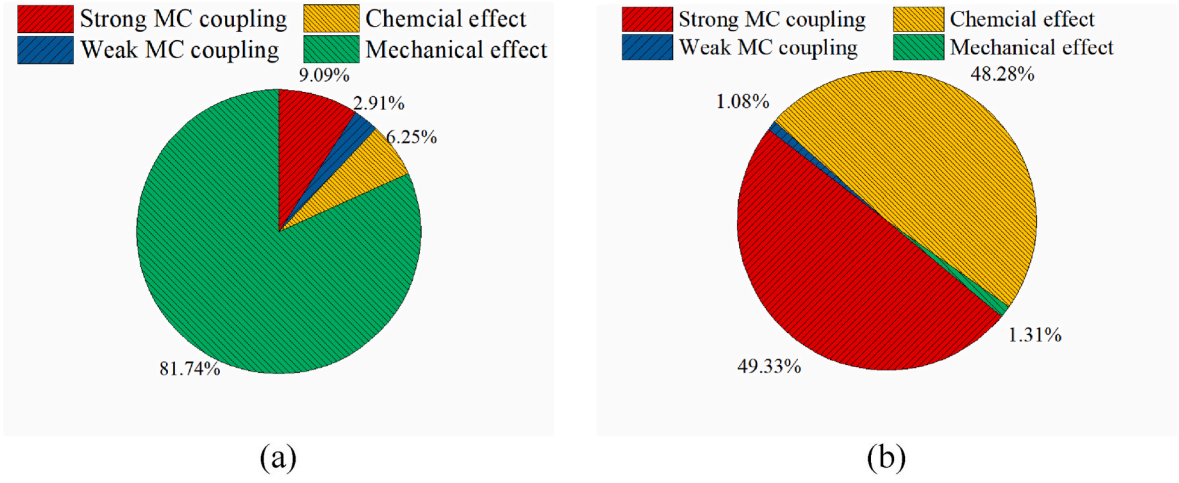

Fig. 23. The relative intensity for positions (a) point A around the injection well and (b) point C far from the injection well.

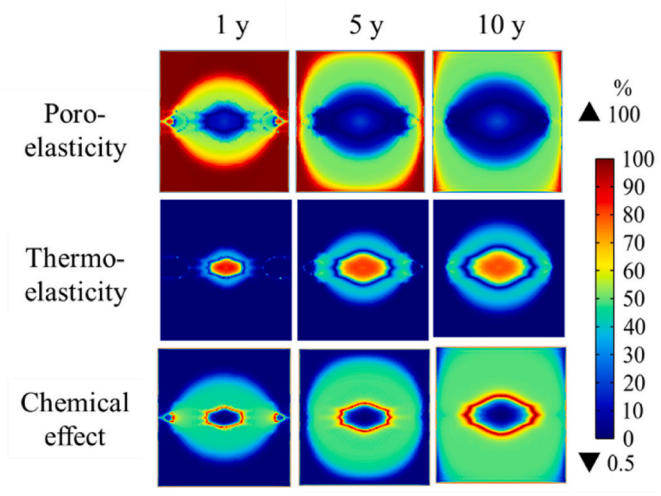

Fig. 24. The distributions of poroelasticity, thermoelasticity and chemical effect contribution ratios on fracture plane F (t = 1, 5 and 10 years).

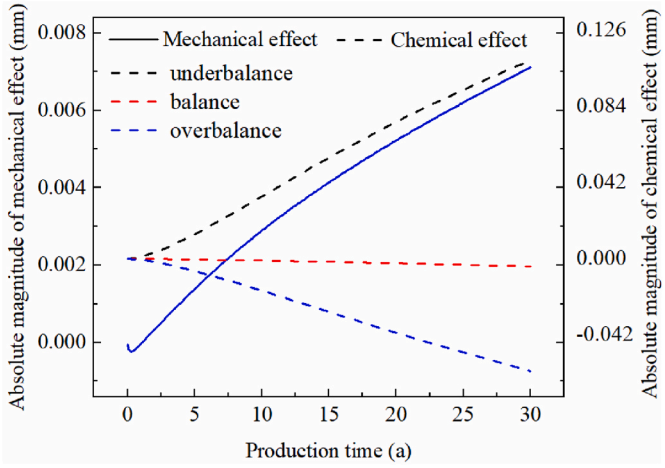

Fig. 25. The influence of injection concentration on the absolute magnitudes of mechanical and chemical effects.

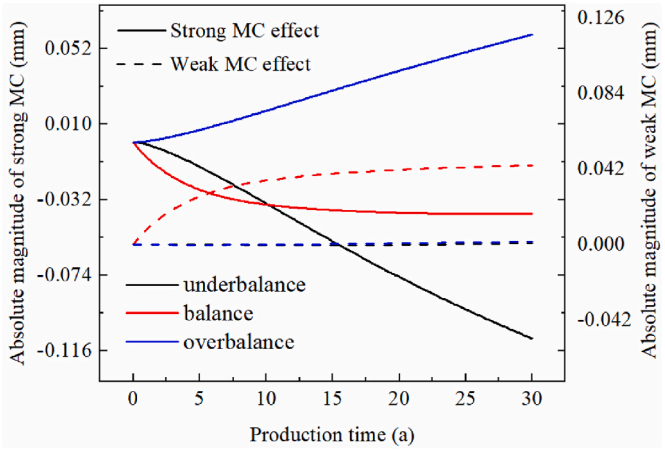

Fig. 26. The influence of injection concentration on the absolute magnitudes of strong MC and weak MC coupling effect.

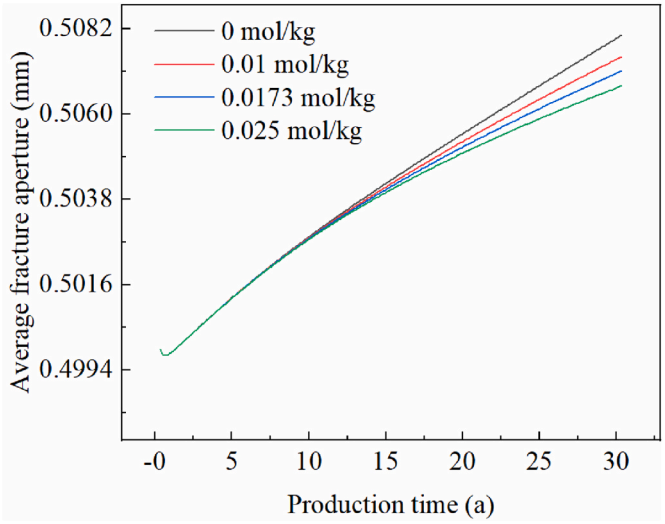

Fig. 27. The effects of injection concentration on the average fracture aperture of plane F.

0.0173 mol/kg which aligns with the equilibrium concentration at the initial temperature of 200 °C. 0 mol/kg signifies underbalanced injection while 20 mol/kg represents overbalanced injection in this section. Fig. 25 indicates variations of chemical injection show minimal impact on the mechanical effect. Balanced injection yields minimal chemical effects due to the absence of reaction trends. However, underbalanced injection results in an amplified chemical effect, enhancing fracture aperture through dissolution reactions. Conversely, overbalanced injection leads to a decrease in chemical effects attributed to precipitation effects. This pattern arises from greater deviations from the equilibrium state, resulting in more pronounced alterations in effect magnitudes.

Fig. 26 depicts the influence of injection solute concentration on the variation of strong MC and weak MC coupling effects. Both under- and over-equilibrium conditions augment the strength of strong MC. Under under-equilibrium conditions, dissolution reactions lead to increased fracture aperture and a negative degree of strong MC effect. Conversely, under over-equilibrium conditions, precipitation reactions result in decreased fracture aperture and a positive degree of strong MC. On the other hand, weak MC coupling remains minimally affected under both circumstances. It is an indirect effect that becomes ignorable when stronger direct constraints and coupling effects are intensified with the arising chemical reactions. Yet, chemical reactions are subdued under equilibrium injection conditions. In this case, little reaction is induced and the constraints from mechanical-chemical effects diminish which causes a reduction in strong MC coupling's contribution to fracture aperture. In contrast, the indirect interaction between MC intensifies. The amplification of mechanical effects enhances heat transfer, which subsequently impacts reactant transport. In turn, reactant transport influences chemical reactions, thereby affecting heat transfer. The indirect interaction between M and C is bolstered. As a result, weak MC coupling is enhanced.

Fig. 27 illustrates the trend of average fracture aperture variation with different injection concentrations. Higher injection concentrations correspond to lower aperture values. Chemical injection concentrations notably modify reservoir properties because of chemical dissolution and precipitation. These results can be explained and quantitated by the above multi-physics effect magnitude theory: the alternation of injection concentration mainly changes the magnitudes of chemical, strong MC coupling, and weak MC coupling effects. Additionally, alterations in fracture aperture yield variations in pressure and temperature as depicted in Fig. 28. Elevated injection concentrations lead to greater pressure differentials and temperatures. The thermal breakthrough could be relieved.

The numerical results of the influence of injection concentration on the magnitudes of multi-physical effects and thermal response are summarized in Table 5 (Cao, 2023a, 2023b). The multi-physics action degree theory provides a quantitative framework for assessing the magnitudes of diverse physical and coupling effects. It offers insights into parameter roles during geothermal operations, clarifying dominant factors shaping reservoir behavior and guiding operational parameter decisions for desired objectives.

5. Conclusions

This study introduces a quantitative assessment of mechanical, chemical, strong MC coupling, and weak MC coupling impacts on EGS reservoir characteristics. The approach is derived from the fracture aperture difference of TH, THM, THC, THM + C, and THMC coupling models. The key conclusions are made as follows.

- The variations of fracture aperture are the combined results of four effects. The mechanical effect increases fracture aperture, while the chemical effect decreases it during underbalanced injection. Strong MC coupling contributes to an enlarged aperture. The weak MC coupling effect indicates a minor influence on fracture variation. Strong MC coupling and chemical effects exhibit a strong negative correlation, where the chemical effect directly triggers strong MC coupling.
- Temporally, mechanical effects dominate in the early stage while chemical effects dominate later. Thus, the initial concern lies in mechanical damage while the subsequent focus shifts to chemical plugging and scaling. Spatially, mechanical-driven and chemical-driven regions emerge during stable production. The former governs the area between injection and production wells whereas the latter controls regions distant from injection wells. Operators can manipulate operational strategies to induce directional changes in reservoir characteristics for both proximal and distant wells.
- Injection solute concentration alters fracture aperture by mainly changing chemical, strong MC coupling, and weak MC coupling effects. Higher injection concentration leads to increased pressure difference and delayed thermal breakthrough.

The multi-physics effect degree theory provides valuable insights into the interconnected thermos-hydro-mechanical-chemical coupling mechanisms. The directional adjustments of operation parameters can be obtained for better performance. The approach holds promise for

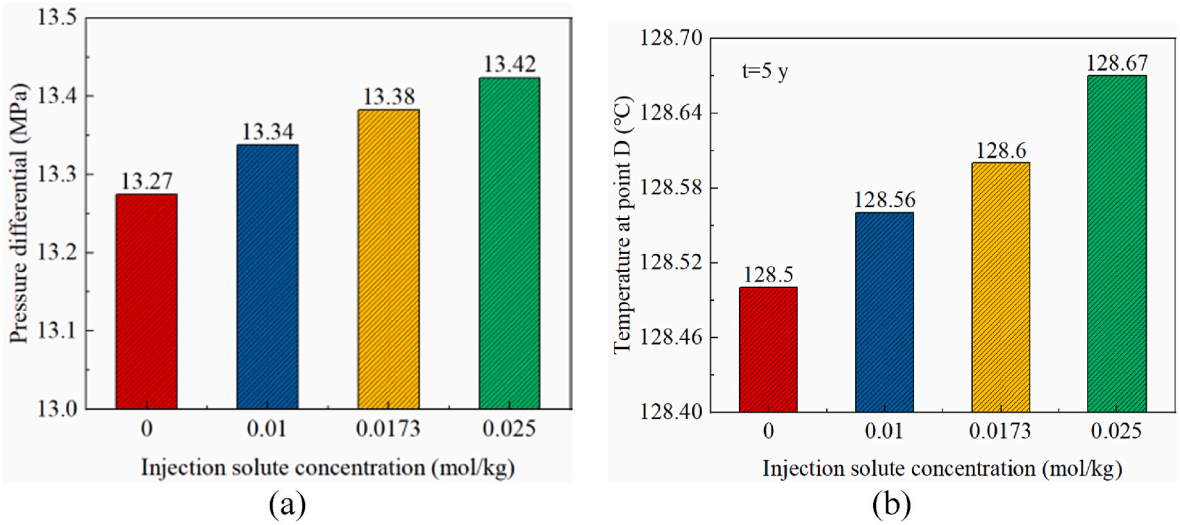

Fig. 28. The influence of injection solute concentrations on (a) pressure differential and (b) local temperature of point D around the production well.

Table 5
A summary of the influence of injection concentration on multi-physical effects and average fracture aperture.

Injection concentration	Absolute magnitudes and fracture aperture (t = 30 year)				
	Strong MC coupling (mm)	Weak MC coupling (mm)	Chemical (C) effect (mm)	Mechanical (M) effect (mm)	Average fracture aperture (mm)
Underbalance (0 mol/kg)	−0.10926	0.000914	0.00711	0.10927	0.50803
Balance (0.0173 mol/kg)	−0.03989	0.04405	0.00711	−0.00416	0.50711
Overbalance (0.025 mol/kg)	0.05987	0.00155	0.00711	−0.06181	0.50672

addressing multi-physics coupling issues in other geo-energy scenarios, like CCUS and hydrogen storage. Nonetheless, limitations arise when the model is applied to a real system. The reservoir model is ideal for now with homogeneous property distribution. Heterogeneous porosity and permeability distributions should be further considered where the geo-statistics method and uncertainty quantity analysis can be conducted. Although a discrete fracture network is employed, the inclusion of more complex fractures is warranted. Regarding chemical reactions, this work focuses solely on the silica-water reaction, given silica's prominence in Hot Dry Rock. In reality, additional reactions such as the calcite-water reaction should be considered due to the diverse mineral content in the reservoir (Ji et al., 2023a, 2023b). The mechanical-chemical coupling effects may vary when different chemical reactions are included, affecting the magnitudes of multi-physics coupling. Shear deformation (Cao et al., 2023) can also be considered further to improve the THMC fully coupled model. With the increasing complexity of the reservoir system, convergence issues arise and simulation computation should be concerned.

CRediT authorship contribution statement

Guofeng Song: Conceptualization, Data curation, Investigation, Methodology, Software, Writing – original draft. **Yu Shi:** Funding acquisition, Supervision, Writing – review & editing. **Fuqiang Xu:** Visualization, Writing – review & editing. **Xianzhi Song:** Conceptualization, Funding acquisition, Supervision, Writing – review & editing. **Gensheng Li:** Project administration, Supervision. **Gaosheng Wang:** Visualization, Writing – review & editing. **Zehao Lv:** Writing – review & editing.

Declaration of competing interest

The authors declare that they have no known competing financial interests or personal relationships that could have appeared to influence the work reported in this paper.

Data availability

Data will be made available on request.

Acknowledgments

The authors would like to acknowledge the Project supported by Major Program of the National Natural Science Foundation of China (Grant No. 52192621), National Key Scientific Research Instrument Research Project of NSFC (No. 51827804), National Natural Science Foundation of China (Grant No. 52104034), National Natural Science Foundation of China (Grant No. 52304057), and China National Post-doctoral Program for Innovative Talents (Grand No. BX20230428).

Nomenclature

EGS	enhanced geothermal system
HDR	hot dry rock
MC	mechanical-chemical
SMC	strong mechanical-chemical coupling
SRV	stimulated reservoir volume
THM + C	thermo-hydro-mechanical-chemical coupling without MC
THMC	thermo-hydro-mechanical-chemical fully coupled
WMC	weak mechanical-chemical coupling

Subscripts

0	initial value
eff	effective coefficient
eq	equilibrium
f	fluid
m	solid matrix

Symbols

C	silica mineral content in the reservoir
C_f	fluid compressibility, Pa^{-1}
C_p	specific heat capacity, J/(kg·K)
D	solute diffusion coefficient in the matrix, m^2/s
e	volume strain
E	young's modulus, Pa
G	shear modulus, Pa
k_+	reaction rate constant, mol/(m^2·s)
K_d	drained bulk modulus of the porous matrix, MPa
k_f	permeability of the fracture, m^2
k_m	permeability of the rock matrix, m^2
K_n	normal stiffness of fracture, Pa
M	molar mass, kg/mol
q	mass rate, kg/s
Q_1	mass flux from rock matrix to fractures, kg/(m^2·s)
Q_2	heat flux between the matrix and fracture, W/m^3
Q_3	solute flux from the matrix to the fracture, mol/(m^3·s)
R	reaction rate, mol/(m^2·s)
S	storage coefficient, Pa^{-1}
w	moles of silica per unit mass of rock, mol/kg

Greek symbols

σ	stress, Pa
ν	poisson's ratio
α_B	Biot-Willis coefficient
α_T	thermal expansion coefficient, K^{-1}
β	irregularity of fracture surface
δ_{ij}	kronecker symbol
λ	heat conductivity, W/(m·K)
μ_f	fluid viscosity, Pa·s
ρ	density, kg/m^3
τ	tortuosity factor
φ	porosity
∇	gradient operator
Δ	difference operator

Variables

AS	absolute strength of multi-physics effects
d_h	hydraulic aperture, m
u_c	chemical aperture, m
c	silica concentration in the fluid, mol/kg
d_c	total aperture without mechanical aperture, m
d_f	total fracture real aperture, m
p	pore pressure, Pa
RS	relative strength of multi-physics effects
T	temperature, K

u displacement, m
t time, s

Appendix A

Herein, the THMC model for geothermal production is established with the fracture aperture as the coupling node. Fig. A1 shows the coupling relationships among four fields. Detailed equations can be found below.

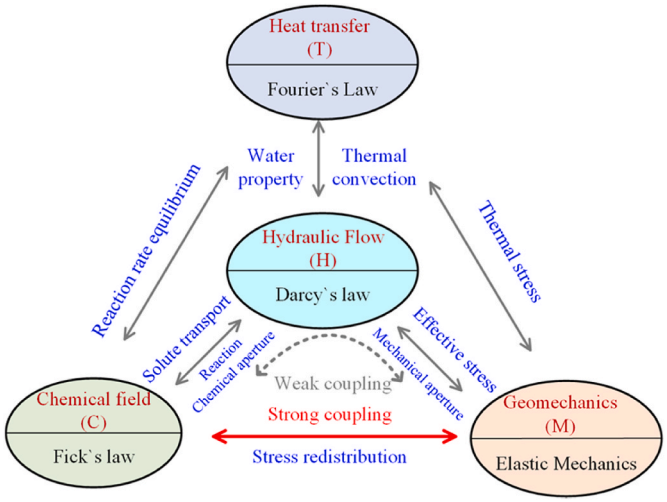

Fig. A1. The coupling relationship among hydraulic flow, heat transfer, geomechanics and chemical field.

A. *Fluid flow*

Darcy's law describes the fluid flow in the rock matrix and fractures:

$$\vec{u} = -\frac{k_m}{\mu_f}\left(\nabla p + \rho_f g \nabla z\right) \tag{9}$$

$$\rho_f S_m \frac{\partial p}{\partial t} + \nabla \cdot \left(\rho_f \vec{u}\right) = -\rho_f \alpha_B \frac{\delta e}{\delta t} \tag{10}$$

$$\vec{u}_f = -\frac{k_f}{\mu_f}\left(\nabla_t p + \rho_f g \nabla_t z\right) \tag{11}$$

$$d_f \rho_f S_f \frac{\partial p}{\partial t} + \nabla_t \cdot \left(d_f \rho_f \vec{u}_f\right) = -d_f \rho_f \alpha_B \frac{\delta e}{\delta t} + Q_1 \tag{12}$$

$$Q_1 = \left(-\frac{\rho_f k_m}{\mu_f}\left(\nabla_n p + \rho_f g \nabla_n z\right)\right)\Big|_{upper} - \left(-\frac{\rho_f k_m}{\mu_f}\left(\nabla_n p + \rho_f g \nabla_n z\right)\right)\Big|_{down} \tag{13}$$

where $\boldsymbol{u_m}$ (m/s) and $\boldsymbol{u_f}$ (m/s) are the flow velocity in the matrix and fracture respectively. k_m (m^2) and k_f (m^2) represent the permeability of the rock matrix and fracture separately. μ_f (Pa·s) is the fluid viscosity. p (Pa) is the pore pressure. ρ_f (kg/m^3) is fluid density and t (s) is time. e is the volume strain which can be computed by the deformation equation hereinafter. d_f (m) is the fracture real aperture that denotes fracture -normal deformation. ∇_t is the gradient operator along the tangential direction of the fracture. Q_1 ($kg/(m^2 \cdot s)$) indicates the mass flux from rock matrix to fractures. ∇_n is the gradient operator along the normal direction of the fracture. α_B means the Biot-Willis coefficient which represents the influence of pore pressure on the rock stress (Biot, 1962). S (Pa^{-1}) is the storage coefficient that considers the fluid and rock compressibility and is expressed as:

$$S = \varphi C_f + (\alpha_B - \varphi)\frac{1 - \alpha_B}{K_d} \tag{14}$$

where φ is the porosity and C_f (Pa^{-1}) is the fluid compressibility. φ_f and φ_m are porosity for fracture and matrix respectively. K_d (MPa) is the drained bulk modulus of the porous matrix. The fracture permeability k_f (m^2) can be expressed by cubic law. It is modified by introducing the transformation between the hydraulic opening and the real opening as follows (Witherspoon et al., 1979):

$$k_f = \frac{{d_h}^2}{12} = \frac{\left(d_{h0} + \beta\left(d_f - d_{f0}\right)\right)^2}{12} \tag{15}$$

where d_h (m) is the hydraulic aperture that is used to compute the fracture conductivity. d_{h0} (m) and d_{f0} (m) represent the initial hydraulic aperture

and initial geometric aperture respectively. β is the coefficient describing the transformation of two kinds of apertures. It denotes the irregularity of the fracture surface with a range generally from 0.5 to 1 (Witherspoon et al., 1979).

B. Heat transfer

Heat transfer in the matrix and fracture can be expressed as follows:

$$\left(\rho C_p\right)_{eff,m}\frac{\partial T}{\partial t}+\rho_f C_{p,f}\vec{u}\cdot\nabla T-\nabla\cdot\left(\lambda_{eff,m}\nabla T_f\right)=0 \tag{16}$$

$$d_f\left(\rho C_p\right)_{eff,f}\frac{\partial T}{\partial t}+d_f\rho_f C_{p,f}\vec{u}_f\cdot\nabla_t T-\nabla_t\cdot\left(d_f\lambda_{eff,f}\nabla_t T_f\right)=Q_2 \tag{17}$$

$$Q_2=\left(\rho_f C_{p,f}(\vec{u}\cdot\vec{n})T-\lambda_{eff,m}\nabla_n T\right)|_{upper}-\left(\rho_f C_{p,f}(\vec{u}\cdot\vec{n})T-\lambda_{eff,m}\nabla_n T\right)|_{down} \tag{18}$$

where T (K) is the temperature of rock and fluid. The second term represents the heat convection and the third term denotes the heat conduction on the left part of equations (9) and (10). $C_{p,f}$ (J/(kg·K)) is the specific heat capacity of the fluid. Q_2 (W/m^3) means the heat flux between the matrix and fracture, which equals the difference between the normal heat flux from the matrix at the upper and lower fracture face. $(\rho C_p)_{eff}$ (J/(K·m^3)) and λ_{eff} (W/(m·K)) are the effective volumetric heat capacity and heat conductivity respectively. They can be expressed based on the volume averaging method:

$$\left(\rho C_p\right)_{eff}=\varphi\rho_f C_{p,f}+(1-\varphi)\rho_s C_{p,m} \tag{19}$$

$$\lambda_{eff}=\varphi\lambda_f+(1-\varphi)\lambda_m \tag{20}$$

where ρ_m (kg/m^3), $C_{p,m}$ (J/(kg·K)), λ_f (W/(m·K)) and λ_m (W/(m·K)) are solid rock density, rock specific heat capacity, fluid heat conductivity and solid heat conductivity respectively.

C. Mechanical deformation

Rock deformation is expressed by the following equations:

$$2Gu_{i,jj}+\frac{2Gv}{1-2v}u_{j,ji}-\alpha_B p\delta_{ij}-3K_d\alpha_T(T-T_0)+F_i=0 \tag{21}$$

where u (m) means the rock displacement and v is Poisson's ratio. α_T (K^{-1}) is the thermal expansion coefficient. T_0 (K) is the initial temperature. δ_{ij} is kronecker symbol. F_i (N/m^3) is the body force per unit volume. G (Pa) is the shear modulus and K_d (Pa) is the volume modulus. They can be obtained by young's modulus E (Pa) and Poisson's ratio as $G=E/2(1+\nu)$ and $K_{\mathrm{d}}=E/3(1-2\nu)$. Volumetric strain e is expressed as follows:

$$e=\frac{\sigma_e}{K_d}=\left(\frac{\sigma_1+\sigma_2+\sigma_3}{3}+\alpha_B\mathrm{p}\right)\Big/K_d \tag{22}$$

where σ_e (Pa) is effective volumetric stress. σ_1, σ_2, and σ_3 denote the first, second and third main stress respectively.

D. Chemical solute transportation

There occurs reactant convection and diffusion when the solute is carried by the fluid. The solute transportation in rock matrix is described as follows:

$$\frac{\partial\left(\varphi_m\rho_f c\right)}{\partial t}+\vec{u}\cdot\nabla\left(\rho_f c\right)-\nabla\cdot\left(D_{eff,m}\nabla\left(\rho_f c\right)\right)=0 \tag{23}$$

$$D_{eff,m}=\frac{\varphi_m}{\tau_m}D_m,\tau_m=\varphi_m{}^{-1/3} \tag{24}$$

where c (mol/kg) is silica concentration in the fluid. $\vec{u}\cdot\nabla(\rho_f c)$ indicates the convective process and $-\nabla\cdot(D_{eff,m}\nabla(\rho_f c))$ denotes the solute diffusion in the matrix. $D_{eff,m}$ (m^2/s) is the effective diffusion coefficient controlled by Millington and Quirk model (Millington and Quirk, 1961). D_m (m^2/s) is the solute diffusion coefficient in the matrix. τ_m is the tortuosity factor for the matrix accounts for the reduced diffusivity since the solid grains impede Brownian motion (Millington and Quirk, 1961). Similarly, the convection and diffusion of solute in the fracture can be written as (Pandey et al., 2014):

$$d\frac{\partial\left(\varphi_f\rho_f c\right)}{\partial t}+d\vec{u}_f\cdot\nabla_t\left(\rho_f c\right)-\nabla_t\cdot\left(dD_{eff,f}\nabla_t\left(\rho_f c\right)\right)=dR+Q_3 \tag{25}$$

$$Q_3=\left((\vec{u}\cdot\vec{n})\rho_f c-D_{eff,m}\nabla_n\left(\rho_f c\right)\right)|_{upper}-\left((\vec{u}\cdot\vec{n})\rho_f c-D_{eff,m}\nabla_n\left(\rho_f c\right)\right)|_{down} \tag{26}$$

$$D_{eff,f}=\frac{\varphi_f}{\tau_f}D_f,\tau_f=\varphi_f{}^{-1/3} \tag{27}$$

where Q_3 (mol/(m^3·s)) means the solute flux from the matrix to the fracture. $D_{eff,f}$ ((m^2/s)) denotes the effective diffusion coefficient in the fracture. R (mol/(m^2·s)) represents the solute source contributed by the chemical reaction at the fracture surface. It originates from the silica reaction around the

interface between the matrix and fracture zone.

E. Evolution of fracture aperture

Total fracture aperture is the combination of mechanical and chemical aperture. Mechanical aperture is induced by matrix elastic deformation. It follows the effective stress principle (Guo et al., 2020). It is defined as:

$$u_m = \frac{\sigma_{n,frac} - p}{k_n} \tag{28}$$

where $\sigma_{n,frac}$ is normal stress on the fracture plane. The stress can be obtained by elastic equations as shown in (21). K_n (Pa) and u_m (m) are normal stiffness and normal displacement. To simplify the simulation process, shear dilation is not considered here (Salimzadeh and Nick, 2019; Shi et al., 2019b).

Chemical aperture is induced by silica mineral dissolution or precipitation. The chemical equation is $SiO_{2(s)} + 2H_2O \Leftrightarrow H_4SiO_4$ (Rimstidt and Barnes, 1980). The reaction rate R (mol/(m^2·s)) is (Rimstidt and Barnes, 1980; Song G. et al., 2022a):

$$R = k_+ \left(1 - \frac{c}{c_{eq}}\right) \tag{29}$$

$$\log_{10} c_{eq} = 0.3380 - 7.8890 \times 10^{-4} T - \frac{840.1}{T} \tag{30}$$

$$\log_{10} k_+ = -0.369 - 7.890 \times 10^{-4} T - \frac{3438}{T} \tag{31}$$

where c_{eq} (mol/kg) is the equilibrium concentration of amorphous silica in fluid and k_+ (mol/(m^2·s)) is the reaction rate constant. It is undersaturation when c is lower than c_{eq} while it is oversaturation if c is larger than c_{eq}. Undersaturation leads to silica dissolution while oversaturation results in silica precipitation. Therefore, the chemical aperture u_c (m) can be obtained by:

$$\frac{\delta d_c}{\delta t} = \frac{R}{\rho_s w} \tag{32}$$

$$u_c = d_c - d_{f0} \tag{33}$$

where d_c (m) is the total aperture without consideration of mechanical aperture. w (mol/kg) is the number of moles of silica per unit mass of rock, which is defined as C/M. C and M (kg/mol) denote the silica mineral content in reservoir and molar mass respectively. M is 0.03 (kg/mol) for SiO_2. The positive R means that dissolution occurs while the negative R represents that perception takes place. u_c is the chemical aperture which is alternation caused by a chemical reaction without considering the confinement from surrounding rocks. In reality, u_c should be confined by the surrounding rocks. Extra fracture stress should be applied to support u_c. The transformation from the chemical aperture to the stress was made as Equation (34).

$$\sigma'_{n,frac} = K_n \times u_c \tag{34}$$

The updated stress $\sigma'_{n,frac}$ (Pa) is then employed to the next time step and input to equations (21) and (34).

Contact aperture is also not included due to the difficulty of getting the details of the fracture surface. Hence, the equivalent aperture is employed. The variation of fracture is the combined action of chemical and mechanical effects. The total fracture aperture d_f equals the summation of chemical u_c, mechanical u_m, and initial fracture width d_{f0}.

$$d_f = d_{f_0} + u_m + u_c \tag{35}$$

As presented by Salimzadeh and Nick (2019), the simple mathematic summation of the chemical and mechanical aperture is referred to as loose coupling, denoted by THM + C. This type of coupling doesn't contain the influence between chemical and mechanical action, which means they are separate. In fact, fracture surface stress can be altered due to the existence of the chemical aperture. One reason is the change in fracture surface bearing performance. As a result, the mechanical aperture is changed. It is necessary to introduce the coupling between the chemical and mechanical action. Here, u_c is regarded as the input to the u_n. A new mechanical equilibrium is satisfied. The mechanical aperture is updated. This type of strong coupling model is referred to as the THMC model where the mechanochemical coupling is covered. In this case, the fracture permeability k_f (m^2) can be expressed by a modified cubic law (Witherspoon et al., 1979). The fracture is impermeable when its value is 0.

Fig. A1 indicates the mechanical-chemical (MC) coupling. It refers to the interaction between the mechanical and chemical fields. It can be categorized into strong and weak coupling effects. In equation (34), the strong MC coupling where deformation induced by chemical reactions triggers stress redistribution that leads to changes in the mechanical aperture. Weak MC coupling operates indirectly, as illustrated by the grey lines in Fig. A1. Stress-induced deformation modifies fracture aperture and permeability, influencing convective heat transfer. This, in turn, impacts flow and temperature fields. Fluctuations in temperature and pressure lead to variations in the transport of reaction concentrations and chemical reactions, ultimately affecting reaction-induced deformation. Conversely, the chemical field indirectly influences stress deformation through the thermal and hydraulic fields. Weak MC coupling involves the interplay between stress and chemical fields indirectly through flow and heat transfer.

References

Anyim, K., Gan, Q., 2020. Fault zone exploitation in geothermal reservoirs: production optimization, permeability evolution and induced seismicity. Advances in Geo-Energy Research.

Baria, R., Baumgärtner, J., Rummel, F., Pine, R.J., Sato, Y., 1999. HDR/HWR reservoirs: concepts, understanding and creation. Geothermics 28 (4–5), 533–552.

Biot, M.A., 1962. Mechanics of deformation and acoustic propagation in porous media. J. Appl. Phys. 33 (4), 1482–1498.

Cao, D., 2023a. Enhanced buckling strength of the thin-walled continuous carbon fiber–reinforced thermoplastic composite through dual coaxial nozzles material extrusion process. Int. J. Adv. Des. Manuf. Technol. 128 (3–4), 1305–1315.
Cao, D., 2023b. Fusion joining of thermoplastic composites with a carbon fabric heating element modified by multiwalled carbon nanotube sheets. Int. J. Adv. Des. Manuf. Technol. 128 (9), 4443–4453.
Cao, D., Bouzolin, D., Lu, H., Griffith, D.T., 2023. Bending and shear improvements in 3D-printed core sandwich composites through modification of resin uptake in the skin/core interphase region. Compos. B Eng. 264, 110912.
Cao, W., Huang, W., Jiang, F., 2016. A novel thermal–hydraulic–mechanical model for the enhanced geothermal system heat extraction. Int. J. Heat Mass Tran. 100, 661–671.
Chen, Y., Ma, G., Wang, H., 2018. The simulation of thermo-hydro-chemical coupled heat extraction process in fractured geothermal reservoir. Appl. Therm. Eng. 143, 859–870.
Cristea, V.M., Băgiu, E.D., Agachi, P.Ş., 2010. Simulation and Control of Pollutant Propagation in Someș River Using COMSOL Multiphysics, Computer Aided Chemical Engineering. Elsevier, pp. 985–990.
Cui, Q., Shi, Y., Zhang, Y., Wu, R., Jiao, Y., 2023. Comparative study on the thermal performance and economic efficiency of vertical and horizontal ground heat exchangers. Advances in Geo-Energy Research 7 (1), 7–19.
DiPippo, R., 2012. Geothermal Power Plants: Principles, Applications, Case Studies and Environmental Impact. Butterworth-Heinemann.
Ebrahimi, M., Ameri, M.J., Vaghasloo, Y.A., Sabah, M., 2022. Fully coupled thermo-hydro-mechanical approach to model fracture response to injection process in enhanced geothermal systems using displacement discontinuity and finite element method. J. Petrol. Sci. Eng. 208, 109240.
Guo, T., Tang, S., Sun, J., Gong, F., Liu, X., Qu, Z., Zhang, W., 2020. A coupled thermal-hydraulic-mechanical modeling and evaluation of geothermal extraction in the enhanced geothermal system based on analytic hierarchy process and fuzzy comprehensive evaluation. Appl. Energy 258, 113981.
Iooss, B., Lemaître, P., 2015. A Review on Global Sensitivity Analysis Methods. Uncertainty Management in Simulation-Optimization of Complex Systems: Algorithms and Applications, pp. 101–122.
Izadi, G., Elsworth, D., 2015. The influence of thermal-hydraulic-mechanical-and chemical effects on the evolution of permeability, seismicity and heat production in geothermal reservoirs. Geothermics 53, 385–395.
Ji, J., Song, X., Li, S., Xu, F., Song, G., Shi, Y., Yi, J., 2023a. Study on the effect of fracture morphology on fracture deformation based on the thermal-hydraulic-chemical-deformation coupling model. Energy 282, 128628.
Ji, J., Song, X., Song, G., Xu, F., Shi, Y., Lv, Z., Li, S., Yi, J., 2023b. Study on fracture evolution model of the enhanced geothermal system under thermal-hydraulic-chemical-deformation coupling. Energy 269, 126604.
Jiao, K., Han, D., Wang, B., Chen, Y., Bai, B., Gong, L., Yu, B., 2023. Pore-scale modeling of thermal-hydro-mechanical-chemical coupled rock dissolution and fracturing process. J. Clean. Prod., 138391
Lei, Z., Zhang, Y., Zhang, S., Fu, L., Hu, Z., Yu, Z., Li, L., Zhou, J., 2020. Electricity generation from a three-horizontal-well enhanced geothermal system in the Qiabuqia geothermal field, China: Slickwater fracturing treatments for different reservoir scenarios. Renew. Energy 145, 65–83.
Li, G., Huang, Z., Tian, S., Shen, Z., 2010. Research and application of water jet technology in well completion and stimulation in China. Petrol. Sci. 7, 239–244.
Li, G., Ji, J., Song, X., Shi, Y., Li, S., Song, Z., Song, G., Xu, F., 2022. Research advances in multi-field coupling model for geothermal reservoir heat extraction. Energy Rev. 100009.
Li, Q., Ito, K., Wu, Z., Lowry, C.S., Loheide II, S.P., 2009. COMSOL Multiphysics: a novel approach to ground water modeling. Ground Water 47 (4), 480–487.
Li, S., Feng, X.-T., Zhang, D., Tang, H., 2019. Coupled thermo-hydro-mechanical analysis of stimulation and production for fractured geothermal reservoirs. Appl. Energy 247, 40–59.
Lu, S.-M., 2018. A global review of enhanced geothermal system (EGS). Renew. Sustain. Energy Rev. 81, 2902–2921.
Mahmoodpour, S., Singh, M., Turan, A., Bär, K., Sass, I., 2022. Simulations and global sensitivity analysis of the thermo-hydraulic-mechanical processes in a fractured geothermal reservoir. Energy 247, 123511.
McClure, M.W., Horne, R.N., 2014. An investigation of stimulation mechanisms in Enhanced Geothermal Systems. Int. J. Rock Mech. Min. Sci. 72, 242–260.
Millington, R., Quirk, J., 1961. Permeability of porous solids. Trans. Faraday Soc. 57, 1200–1207.
Multiphysics, C., 2017. COMSOL Multiphysics User's Guide. COMSOL AB Burlington, Mass.
Olasolo, P., Juárez, M., Morales, M., Liarte, I., 2016. Enhanced geothermal systems (EGS): a review. Renew. Sustain. Energy Rev. 56, 133–144.
Pan, J., Xi, X., Wu, X., Guo, Q., Ren, F., Cai, M., 2023. Physical properties evolution and microscopic mechanisms of granite modified by thermal and chemical stimulation. Case Stud. Therm. Eng. 41, 102633.
Pandey, S., Chaudhuri, A., Kelkar, S., Sandeep, V., Rajaram, H., 2014. Investigation of permeability alteration of fractured limestone reservoir due to geothermal heat extraction using three-dimensional thermo-hydro-chemical (THC) model. Geothermics 51, 46–62.
Pandey, S., Chaudhuri, A., Rajaram, H., Kelkar, S., 2015. Fracture transmissivity evolution due to silica dissolution/precipitation during geothermal heat extraction. Geothermics 57, 111–126.
Panwar, N.L., Kaushik, S.C., Kothari, S., 2011. Role of renewable energy sources in environmental protection: a review. Renewable and sustainable energy reviews 15 (3), 1513–1524.
Parisio, F., Vilarrasa, V., Wang, W., Kolditz, O., Nagel, T., 2019. The risks of long-term re-injection in supercritical geothermal systems. Nat. Commun. 10 (1), 1–11.
Pianosi, F., Sarrazin, F., Wagener, T., 2015. A Matlab toolbox for global sensitivity analysis. Environ. Model. Software 70, 80–85.
Prajapati, M., Shah, M., Soni, B., 2021. A review of geothermal integrated desalination: a sustainable solution to overcome potential freshwater shortages. J. Clean. Prod. 326, 129412.
Rathnaweera, T.D., Wu, W., Ji, Y., Gamage, R.P., 2020. Understanding injection-induced seismicity in enhanced geothermal systems: from the coupled thermo-hydro-mechanical-chemical process to anthropogenic earthquake prediction. Earth Sci. Rev. 205, 103182.
Rawal, C., Ghassemi, A., 2014. A reactive thermo-poroelastic analysis of water injection into an enhanced geothermal reservoir. Geothermics 50, 10–23.
Rimstidt, J.D., Barnes, H., 1980. The kinetics of silica-water reactions. Geochem. Cosmochim. Acta 44 (11), 1683–1699.
Rohit, R., Kiplangat, D.C., Veena, R., Jose, R., Pradeepkumar, A., Kumar, K.S., 2023. Tracing the evolution and charting the future of geothermal energy research and development. Renew. Sustain. Energy Rev. 184, 113531.
Salimzadeh, S., Nick, H., 2019. A coupled model for reactive flow through deformable fractures in enhanced geothermal systems. Geothermics 81, 88–100.
Sharmin, T., Khan, N.R., Akram, M.S., Ehsan, M.M., 2023. A state-of-the-art review on for geothermal energy extraction, Utilization, and Improvement strategies: Conventional, Hybridized, and enhanced geothermal systems. International Journal of Thermofluids, 100323.
Shi, Y., Song, X., Li, J., Wang, G., Zheng, R., YuLong, F., 2019a. Numerical investigation on heat extraction performance of a multilateral-well enhanced geothermal system with a discrete fracture network. Fuel 244, 207–226.
Shi, Y., Song, X., Wang, G., Li, J., Geng, L., Li, X., 2019b. Numerical study on heat extraction performance of a multilateral-well enhanced geothermal system considering complex hydraulic and natural fractures. Renew. Energy 141, 950–963.
Song, G., Song, X., Ji, J., Wu, X., Li, G., Xu, F., Shi, Y., Wang, G., 2022a. Evolution of fracture aperture and thermal productivity influenced by chemical reaction in enhanced geothermal system. Renew. Energy 186, 126–142.
Song, G., Song, X., Li, G., Shi, Y., Wang, G., Ji, J., Xu, F., Song, Z., 2021. An integrated multi-objective optimization method to improve the performance of multilateral-well geothermal system. Renew. Energy 172, 1233–1249.
Song, G., Song, X., Li, G., Xu, R., Cao, W., Zhao, C., 2021. Multi-objective optimization of geothermal extraction from the enhanced geothermal system in Qiabuqia geothermal field, Gonghe basin. Acta Geologica Sinica-English Edition 95 (6), 1844–1856.
Song, G., Song, X., Xu, F., Li, G., Shi, Y., Ji, J., 2022b. Contributions of thermo-poroelastic and chemical effects to the production of enhanced geothermal system based on thermo-hydro-mechanical-chemical modeling. J. Clean. Prod., 134471
Song, G., Song, X., Xu, F., Li, G., Wang, G., Ji, J., Shi, Y., 2022c. Numerical parametric investigation of thermal extraction from the enhanced geothermal system based on the thermal-hydraulic-chemical coupling model. J. Clean. Prod. 352, 131609.
Song, X., Li, G., Huang, Z., Shi, Y., Wang, G., Song, G., Xu, F., 2022. Review of high-temperature geothermal drilling and exploitation technologies. Gondwana Res.
Song, X., Shi, Y., Li, G., Yang, R., Wang, G., Zheng, R., Li, J., Lyu, Z., 2018. Numerical simulation of heat extraction performance in enhanced geothermal system with multilateral wells. Applied energy 218, 325–337.
Sun, Z., Jiang, C., Wang, X., Lei, Q., Jourde, H., 2020. Joint influence of in-situ stress and fracture network geometry on heat transfer in fractured geothermal reservoirs. Int. J. Heat Mass Tran. 149, 119216.
Taron, J., Elsworth, D., 2009. Thermal–hydrologic–mechanical–chemical processes in the evolution of engineered geothermal reservoirs. Int. J. Rock Mech. Min. Sci. 46 (5), 855–864.
Taron, J., Elsworth, D., 2010. Coupled mechanical and chemical processes in engineered geothermal reservoirs with dynamic permeability. Int. J. Rock Mech. Min. Sci. 47 (8), 1339–1348.
Vik, H.S., Salimzadeh, S., Nick, H.M., 2018. Heat recovery from multiple-fracture enhanced geothermal systems: the effect of thermoelastic fracture interactions. Renew. Energy 121, 606–622.
Witherspoon, P., Amick, C., Gale, J., Iwai, K., 1979. Observations of a potential size effect in experimental determination of the hydraulic properties of fractures. Water Resour. Res. 15 (5), 1142–1146.
Xu, F., Shi, Y., Song, X., Li, G., Song, Z., Li, S., 2023. The characteristics and laws of fracture damage in the long-term production process of high-temperature geothermal resources. Rock Mech. Rock Eng. 56 (1), 275–299.
Yang, R., Wang, Y., Song, G., Shi, Y., 2023. Fracturing and thermal extraction optimization methods in enhanced geothermal systems. Advances in Geo-Energy Research 9 (2).
Zhang, Y., Hu, X., Wu, X., Li, G., Li, J., Tian, S., Shen, K., 2023. A study of swirling jet drilling and its specific energy for hydrate-bearing sediments. SPE J. 28 (2), 804–818.
Zhu, J., Liu, G., Luo, N., Gu, J., Liu, H., Ye, D., 2023. A new fractal model for quantitatively investigating the contribution of microstructural evolution to geothermal extraction. Renew. Energy 211, 42–54.